Mitigation of bias sources for atmospheric temperature and humidity in the mobile Weather & Aerosol Raman Lidar (WALI)

Julien Totems, Patrick Chazette and Alexandre Baron

[1]{Laboratoire des Sciences du Climat et de l'Environnement, CEA, Gif-sur-Yvette, France}

Correspondence to: J. Totems (julien.totems@cea.fr)

Abstract

Lidars using vibrational and rotational Raman scattering to continuously monitor both the water vapor and temperature profiles in the low and middle troposphere offer enticing perspectives for applications in weather prediction and studies of aerosol/cloud/water vapor interactions by deriving simultaneously relative humidity and atmospheric optical properties. Several heavy systems exist in European laboratories but only recently have they been downsized and ruggedized for deployment in the field. In this paper, we describe in detail the technical choices made during the design and calibration of the new Raman channels for the mobile Weather and Aerosol Lidar (WALI), going over the important sources of bias and uncertainty on the water vapor & temperature profiles stemming from the different optical elements of the instrument. For the first time, the impacts of interference filters and non-common-path differences between Raman channels, and their mitigation, are particularly investigated, using horizontal shots in a homogeneous atmosphere. For temperature, the magnitude of the highlighted biases can be much larger than the targeted absolute accuracy of 1°C defined by the WMO (up to 6°C bias below 300 m range). Measurement errors are quantified using simulations and a number of radiosoundings launched close to the laboratory. After de-biasing, the remaining mean differences are below 0.1 g/kg on water vapor, 1°C on temperature, and RMS differences are consistent with the expected error from lidar noise, calibration uncertainty, and horizontal inhomogeneities of the atmosphere between the lidar and radiosondes.

1 Introduction

Atmospheric temperature and humidity in the low atmosphere are together essential to comprehend weather phenomena and their evolution in a changing climate. Through the effect of relative humidity on aerosol hygroscopicity and cloud formation, they also influence the

1

30   radiative balance of the Earth, generating the largest uncertainties in climate projections (IPCC,

31   2013). For both weather and climate prediction, observation means have evolved tremendously,

32   notably with satellite retrievals of moisture and temperature routinely assimilated in numerical

33   models. Yet remote-sensing techniques from spaceborne missions have difficulties probing the

34   lower troposphere below 2-3 km in altitude, and have vertical resolutions that are too low,

35   greater than 1 km in the lower troposphere (e.g. Prunet et al., 1998; Crevoisier et al., 2014).

36   They are thus unable to resolve temperature inversions and thin dry/humid air masses (e.g.

37   Chazette et al., 2014; Hammann et al., 2015; Totems et al., 2019). Providing complementary

38   profiles of the important thermodynamic variables in the first kilometres of the atmosphere,

39   where most of the water vapour and temperature vertical variability is confined, is of paramount

40   importance for both weather forecast and reducing aerosol-induced uncertainty on climate

41   models (Wulfmeyer et al., 2015).

42   Given their capacity for continuous, well-resolved and precise temperature measurements in

43   the lower troposphere, Vibrational Raman (VR) and Rotational Raman (RR) lidars have

44   emerged as adequate tools in this endeavour. Water vapor profilers are now well-established

45   (from Whiteman et al., 1992 to e.g. Dinoev et al., 2013), whereas temperature profilers have

46   recently become more widespread and powerful (from Cooney, 1972 and Vaughan et al., 1993

47   to e.g. Weng et al., 2018 or Martucci et al., 2021). Without tackling turbulence-scale resolution

48   which is the prerogative of heavier systems like the Raman lidars of the University of

49   Hohenheim (Behrendt et al., 2015), the University of Basilicata (Di Girolamo et al., 2017) or

50   ARTHUS (Atmospheric Raman Temperature and Humidity Sounder, Lange et al., 2019), there

51   is a need for field-deployable instruments capable of fulfilling the breakthrough requirements

52   set by the World Meteorological Organization in terms of accuracy on atmospheric temperature

53   and humidity in the low troposphere (WMO, 2017). Lidar profiles have proven beneficial for

54   both numerical weather prediction (NWP) models (e.g. Adam et al., 2016; Fourrié et al., 2019),

55   the study of dynamic processes in the planetary boundary layer (PBL) (e.g. Behrendt et al.,

56   2015) or interactions between water vapor and aerosols (e.g. Navas-Guzmán et al., 2019). But

57   to obtain the absolute accuracies demanded here, especially that of 1°C or less on temperature,

58   the required accuracy on the lidar channel ratios and their calibration is extremely stringent,

59   and the sources of systematic error seldom discussed in the literature (Behrendt and Reichardt,

60   2000; Simeonov et al., 1999; Whiteman et al., 2012).

61   Within the European lidar landscape, WALI (Weather and Aeorosol Lidar) is a seasoned mobile

62   Rayleigh-Mie-Raman system, "eyesafe" at 355 nm, first deployed during the HyMeX

63   international field campaign and subsequently ChArMEx and PARCS, for aerosol and water

64 vapor profiling (resp. Hydrological cycle in the Mediterranean eXperiment, Chemistry and
65 Aerosol in the Mediterranean Experiment, Pollution in the Arctic System; Chazette et al.,
66 2014b, 2018; Totems et al., 2019; Totems and Chazette, 2016). In its latest evolution, the VR
67 channels have been replaced by a Newton reflector and a polychromator also including RR
68 channels for temperature profiling. On this occasion, we have established that biases due to
69 various sources, in particular from the dependency of spectral filtering on the angle of
70 incidence, detector non-uniformities and other non-common-path differences between Raman
71 channels, may be several times greater than the requirements if left unchecked. Correctible as
72 they are by measuring the ratios of overlap factors on the individual channels, these effects are
73 not reported in the literature of lidar temperature measurements. However, they were bound to
74 appear given the physical characteristics of the systems mentioned hereabove.

75 The aims of this paper are: i) to compile for the first time the sources of systematic error that
76 must be considered and mitigated when using a Raman lidar to profile atmospheric temperature
77 and humidity, ii) to validate WALI as a dependable profiler deployable for field campaigns,
78 satisfying the requirements set by the WMO.

79 The theory of the Raman lidar retrieval of the atmospheric temperature and WVMR, the error
80 budget on these parameters, and the known causes of bias are recalled in section 2, as well as
81 the principle and limitations of the overlap measurement method. In section 3, after
82 summarizing the characteristics of WALI, we propose a sequential review of the components
83 of the lidar chain, characterizing and mitigating the error sources. The results of a calibration
84 and qualification experiment using radiosondes follow in section 4. A conclusion and outlooks
85 are presented in section 5.

86 **2   Theoretical considerations**

87 **2.1   Raman lidar retrieval of humidity and temperature**

88 We will introduce notations by briefly recalling the theory of the retrieval of water vapor content
89 and temperature by the Raman lidar technique; the complete theory has been extensively
90 derived before, by Whiteman et al. (1992) and Behrendt (2005) respectively, among others.

91 The vertical profiles of water vapor mixing ratio (WVMR) r_{H2O} and temperature T are
92 calculated from the ratios of the H_2O / N_2-vibrational Raman (VR) channels and the RR2 (high-
93 J number) / RR1 (low-J number) rotational Raman (RR) channels, respectively:

$$R(z) = \frac{S_{H_2O}(z)}{S_{N_2}(z)} \tag{1}$$

$$Q(z) = \frac{S_{RR2}(z)}{S_{RR1}(z)} \tag{2}$$

94   Signals $S_j(z)$ of Raman channels j have all been previously averaged over the required altitude

95   and time to improve the signal to noise ratio (SNR), and corrected for i) electronic baseline

96   variations by subtracting a baseline recorded every few profiles with detector (photomultiplier

97   tube, PMT) gain set to zero, ii) the sky background mean value assessed on pre-trigger or post-

98   signal samples, iii) PMT gain variations (allowed on the VR channels to optimize daytime

99   dynamic range, eg. Chazette et al. (2014b)), iv) known leakage of the elastic return in the RR

100   filters (Behrendt and Reichardt, 2000). $S_j(z)$ are thus expressed as:

$$S_j(z) = \frac{1}{G_j(U_j)}\big(S_{j,raw}(z) - \hat{L}_j(z) - \hat{B}_j\big) - \hat{\varepsilon}_j S_{elas}(z) \tag{3}$$

101   where G_j is the channel gain controlled by PMT voltage U_j, $S_{j,raw}$ is the raw lidar signal, $\hat{L}_j$ is

102   the estimated baseline, $\hat{B}_j$ is the estimated sky background parasitic signal, $\hat{\varepsilon}_j$ is the estimated

103   residual transmittance of the emitted laser wavelength through the interference filter (IF) of

104   Raman channel j compared to the elastic channel, and S_{elas} is the elastic signal. $\hat{x}$ denotes the

105   estimate of x.

106   Both R and Q must then also be corrected for the difference of atmospheric transmission

107   between the two Raman channels and the ratio of overlap factors:

$$R'(z) = \frac{\exp\big(\Delta\tau(z)\big)}{\widehat{OR_R}(z)} R(z) \tag{4}$$

$$Q'(z) = \frac{1}{\widehat{OR_Q}(z)} Q(z) \tag{5}$$

108   where $\Delta\tau(z)$ is the difference of optical thickness from the lidar until range z observed between

109   the wavelengths of the two VR channels, and where $\widehat{OR_R}(z)$ and $\widehat{OR_Q}(z)$ are the estimated

110   ratios of the overlap factors of the two VR / RR channels respectively (expressed in section

111   2.4). With an emitted wavelength at 355 nm, $\Delta\tau(z)$ between 387 and 407 nm seldom produces

112   deviations above 5%, and can be efficiently estimated using an average atmospheric density

113   profile for molecular optical thickness and the N_2-Raman channel itself for aerosol optical

114   thickness (e.g. Whiteman, 2003).

The WVMR is simply proportional to the VR scattering ratio between H_2O and N_2, since nitrogen gas has a constant mixing ratio in the troposphere and stratosphere. The temperature is retrieved from the more complex dependency of the RR scattering cross sections between the two channels RR1 and RR2. The respective estimates $\hat{r}_{H_2O}$ and $\hat{T}$ (to be distinguished from the true values without ^) are obtained, after calibration, by:

$$\hat{r}_{H_2O}(z) = \hat{K} R'(z) \tag{6}$$

$$\hat{T}(z) = \hat{f}^{-1}(Q'(z)) \tag{7}$$

where $\hat{K}$ is the estimate of the calibration coefficient for WVMR combining all instrumental constants. Calibration function $\hat{f}$ is the estimate of the temperature dependency of the ratio of RR cross-sections. It takes into account the instrumental constants of the two RR channels. We take the model previously selected for operational purposes by Behrendt (2005):

$$Q' = f(T) = \exp\left(a + \frac{b}{T} + \frac{c}{T^2}\right) \tag{8}$$

with a, b, c the coefficients of a polynomial regression of $\ln(Q')$ as a function of $1/T$. $\hat{K}$ and $\hat{f}$ are obtained by confronting lidar profiles of R' and Q' with collocated in-situ measurements of r_{H2O} and T (e.g. from a radiosounding), aiming for a wide range of values for a better constraint on the calibration.

2.2 Simple error budget

In this section, we will make a first assessment of the acceptable error on R and Q starting from the accuracy requirements for WVMR and temperature profiles, which ensue from each scientific need, as compiled by Wulfmeyer et al. (2015) for key applications. Monitoring, verification (e.g. model qualification or calibration/validation of satellites) and data assimilation purposes can be adequately addressed by a profiler capable of i) <5% noise error and <2-5% bias for water vapor, ii) <1°C noise error and <0.2-0.5°C bias for temperature. In a simple error budget, we can use requirements of $\left(\frac{\Delta r_{H_2O}}{r_{H_2O}}\right)_{max} = 5\%$ for WVMR, and $\Delta T_{max} = 1°C$ for temperature, to give a first idea of the different expectations for the performance of a VR/RR lidar.

Eqs. (4-8) allow to derive constraints on the acceptable relative error on the corrected lidar observables R' and Q', for either random noise or bias, as:

$$\left(\frac{\Delta R'}{R'}\right)_{max} = \left(\frac{\Delta r_{H_2O}}{r_{H_2O}}\right)_{max} \tag{9}$$

$$\left(\frac{\Delta Q'}{Q'}\right)_{max} = \frac{dQ'/dT}{Q'}\Delta T_{max} \tag{10}$$

The relative error on R is equal to the constraint on WVMR, i.e. 5%. An assessment of the relative error on Q is performed considering the RR filter parameters given in Table 2 (section 3) to yield the following numerical application: around $T_0 = 0°C$, $Q'(T_0) = 0.44$ and $dQ'/dT(T_0) = +0.35/100°C$, so that: $\left(\frac{\Delta Q'}{Q'}\right)_{max} = 0.79\% \ \Delta T_{max}(°C)$.

Table 1. Summary of accuracy requirements from Wulfmeyer et al. (2015) and corresponding constraints on ratios R' and Q'. Resulting errors on relative humidity RH at 0°C and 50%RH.

Parameter	Random error	Systematic error (bias)
r_{H2O}	<5% relative	<2-5% relative
T	<1°C	<0.2-0.5°C
R'	<5% i.e. $SNR > 20$	<2-5%
Q'	<0.8% at 0°C i.e. $SNR > 125$	<0.12-0.4% at 0°C
RH	4.3%RH at $T = 0°C$, $RH = 50\%$	1.2-2.9%RH at $T = 0°C$, $RH = 50\%$

The results, summarized in Table 1, have very important implications. In order to fulfill WMO requirements for temperature and WVMR measurements, the Q' ratio must be 6-10 times more accurate than R'. However, Raman cross-sections are larger for the RR channels than for the H$_2$O VR channel. Hence when dealing with a RR+VR lidar rather than a VR system, the main difficulties are not only due to low signal-to-noise ratio but also encompass strong constraints linked to instrumental biases. SNR as used in Table 1 is defined on R and Q at the final resolution, and is calculated from the individual signal variances and means (including laser & sky-background photon noise, detection noise), as:

$$SNR_R = \left(\frac{\text{var}(S_{N_2})}{\langle S_{N_2}\rangle^2} + \frac{\text{var}(S_{H_2O})}{\langle S_{H_2O}\rangle^2}\right)^{-\frac{1}{2}} \tag{11}$$

$$SNR_Q = \left(\frac{\text{var}(S_{RR1})}{\langle S_{RR1} \rangle^2} + \frac{\text{var}(S_{RR2})}{\langle S_{RR2} \rangle^2} \right)^{-\frac{1}{2}} \tag{12}$$

155 SNR_R, typically limited by the H_2O channel, must be above ~20 and SNR_Q must be above ~125
156 to satisfy the requirements given above. Such high values can be reached by increasing the laser
157 power and pulse repetition frequency (PRF), or enlarging the integration over altitude and time,
158 as SNR is usually magnified by the square roots of the energy and number of averaged samples.
159 However, limits on the latter are also set by Wulfmeyer et al. (2015) for the same applications;
160 integration range Δz should be below 100 m in the PBL and 300 m in the lower free troposphere,
161 whereas an integration time Δt between 15 (assimilation and verification) and 60 min
162 (monitoring) is required.

163 We derive the errors expected on RH given those on temperature and WVMR at the bottom of
164 Table 1. Here and in the following, %RH denote absolute percentage units on RH, whereas %
165 denote relative errors. Relative humidity is derived as a function of atmospheric pressure,
166 temperature and WVMR, using standard empirical relationships for the water vapor saturation
167 pressure. Here, we use the Buck equation (Buck, 1981), which is accurate within 0.2% between
168 $-40°C$ and $+100°C$:

$$P_{wv,sat} = 6.1121 \frac{T}{T + 257.14°C} \exp\left(18.678 - \frac{T}{T + 234.5°C} \right) \tag{13}$$

$$RH = \frac{P}{P_{wv,sat}} \frac{r_{H_2O}}{r_{H_2O} + 621.991 \text{ g kg}^{-1}} \tag{14}$$

169 with P pressure and $P_{wv,sat}$ the water vapor saturation pressure in hPa, T temperature in °C.

2.3 Sources of bias

171 Biases arising from inaccurate measurement of any of the estimated factors of Eqs. (3-7), or
172 from a variation after that measurement due to instabilities in the instrument, must also be
173 smaller than the aforementioned values of 2-5% for WVMR and 0.12-0.4% for temperature,
174 the latter being especially difficult to reach. Their impact must be mitigated either by careful
175 design or by precise estimation.

176 The expected (i.e. noiseless) values of R and Q can be detailed as:

$$\overline{R(z)} = \frac{O_{H_2O}(z)}{O_{N_2}(z)} \frac{K_{H_2O}}{K_{N_2}} \frac{\sigma_{H_2O}}{\sigma_{N_2}} r_{H_2O}(z) \tag{15}$$

$$\overline{Q(z)} = \frac{O_{RR2}(z)}{O_{RR1}(z)} \frac{K_2 \sigma_{RR2}(T(z))}{K_1 \sigma_{RR1}(T(z))} \tag{16}$$

177   with $\bar{x}$ denoting the expected value of variable x, K_j, σ_j and $O_j(z)$, the instrumental constant,

178   Raman backscatter cross-section, and overlap factor of channel j, respectively. To simplify our

179   discussion, we choose to incorporate any deviation that affects the ratios without a range-

180   dependence into the instrumental constant ratio, and any deviation with a range-dependence

181   into the overlap ratio.

182   As previously explained, the impact of deviations on variables in Eq. (15) remains tolerable

183   below a few percent, but for the distinctly more constrained temperature retrieval, the variables

184   in Eq. (16) are affected by the following effects that directly induce significant bias:

185   • Laser wavelength drift or filter central wavelength (CWL) drift with temperature both

186   affect the ratios indiscriminately with range. By simulating the variation of Q with the

187   WALI filter parameters (section 3), we find a large impact of a wavelength drift $\Delta\lambda$

188   (measured between the laser on one side and both interference filters on the other side):

189        $dQ/Q \, /d\lambda \approx -0.26 \, \text{pm}^{-1}$ and $\Delta T \approx -0.34°\text{C} \, \text{pm}^{-1} \, \Delta\lambda$, meaning just 3 pm drift in

190   either filter or laser wavelengths can lead to biases above 1°C. That is one of the reasons

191   why the laser must be frequency-stabilized. Also, IFs subjected to fluctuations of local

192   temperature are known to experience CWL drifts; for WALI's filters manufactured by

193   Materion, this amounts to 1.28 pm °C^{-1} (value given by the manufacturer after their

194   material dilation simulation). The temperature of the polychromator must thus be kept

195   stable within 1°C for this bias to become negligible.

196   • Filter CWL variation with angle of incidence (AOI) on the IF generates a channel

197   transmittance variation which is range-dependent, and different for each filter. Indeed,

198   this variation ΔCWL is approached by (e.g. Hayden Smith and Smith, 1990):

$$\Delta CWL(\theta') \approx CWL \frac{\theta'^2}{2n_{eff}^2} \tag{17}$$

199   where CWL is the filter central wavelength, θ' is the angle of incidence on the filter

200   (assumed small), and n_{eff} is the effective refractive index of the filter. For the RR1 filter

201   ($n_{eff} = 1.62$), we obtain as much as $\Delta CWL(\theta') \approx 43 \, \text{pm} \, \theta'(°)^2$. The problem stems from

202   the fact that because the filter is in the pupil plane, after collimation of the received

203   beam, each angle of incidence corresponds to a different point in the focal plane of the

receiver, which in turns corresponds to a field angle θ of the lidar, as seen on Figure 1 a). Aperture number conservation across the receiving optical system imposes

$$\theta' = \frac{f}{f'}\theta > \frac{D_{rec}}{D_{IF}}\theta \tag{18}$$

where f and f' are the receiver/recollimation focal lengths, D_{rec} and D_{IF} are the receiver and IF diameters. For a 150-mm diameter receiver using a 1-inch diameter (22 mm clear aperture) IF, we obtain at least $\theta' = 0.39°$ for a $\theta = 1$ mrad field angle, producing $\Delta CWL(\theta') \approx 6.6\,pm$ and already $\Delta T \approx 2,2°C$. Note that the impact gets proportionately larger with the diameter of the receiver. Because the optical path of each channel is independently aligned, this always induces different overlap factors even when sharing the same telescope. This large effect must be calibrated and corrected, yet its impact was never discussed before in the RR lidar literature, despite being three times as large in other systems with 450 mm receivers. This impact can be mitigated by attacking the filters at normal incidence, where the derivative of CWL as a function of AOI (see Eq. (17)) is minimal.
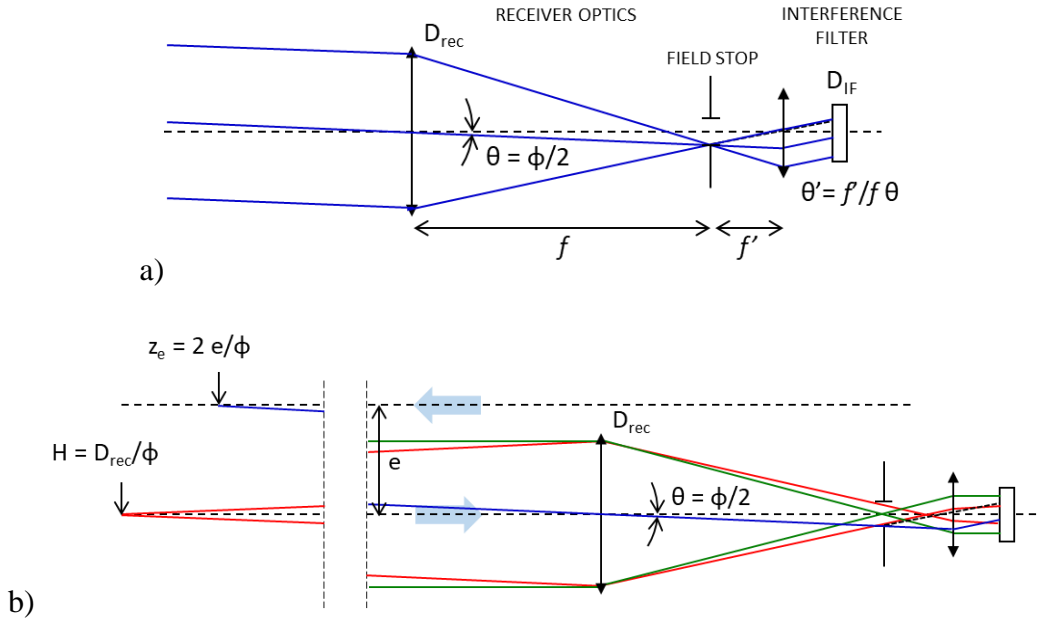

a)

b)

Figure 1. a) Definition of useful parameters for field angle θ and filter angle of incidence θ' calculations. f: receiver focal length, D_{rec}: receiver diameter, ϕ: full lidar field-of-view, f': collimation focal length, D_{IF}: IF diameter. b) Definition of metrics for overlap calculations. e: emitter-receiver separation, H: hyperfocal distance, z_e: entry distance of laser into field-of-view. Green/red/blue lines represent rays from infinity/finite distance/offset emitted beam, respectively.

- Detector response non-uniformity up to ±12%, both as a function of impact point on the active surface and of angle of incidence, is now specified on the cathodes of PMTs used at 400 nm wavelength (Hamamatsu (2007), Section 4.3.3). The amplitude was found to be much larger by Simeonov et al. (1999), with significant impact. This effect has been bluntly limited in all our lidars by putting the cathode plane as far as possible before the focal plane, while still avoiding vignetting. It can still be responsible for differences of overlap factors between channels.

- Uncalibrated PMT gain or digitizer baseline variations will of course induce bias in the channel system constants. We will see how to mitigate these effects.

- Slight variations of overlap or channel transmittance after calibration will be directly responsible for bias. In the next sub-section, we discuss how they can appear.

2.4 Overlap measurement with horizontal shots and limitations

Range-dependent biases influence the lower part of the lidar profiles exactly like the overlap factors. They significantly impact the profiles up to a given range from the emitter, depending on the characteristics of the receiving optics as seen above, but also on the quality of the alignments, which is seldom twice the same. Two methods are used in the literature to approximate the actual overlap factors of a Raman lidar: i) an iterative Klett inversion of elastic and Raman channels sharing the same telescope is easy to achieve (Wandinger and Ansmann, 2002) but inefficient when non-common path errors are involved, whereas ii) the method of aiming the lidar horizontally (e.g. Sicard et al., 2002; Chazette and Totems, 2017) is sometimes impractical but more direct and yields more accurate results in an horizontally homogeneous atmosphere over a range of 1 to 2 km. In the context of RR measurements, it is necessary to implement the latter, and also to measure the ratios of overlap factors, rather than the overlap factors themselves, thus avoiding errors due to an imprecise estimation of atmospheric extinction.

Considering a horizontal line of sight in a supposedly homogeneous atmosphere, the expected values of ratios R and Q can be expressed as:

$$\overline{R(z)} = R(z_\infty) \frac{O_{H_2O}(z)}{O_{N_2}(z)} \exp(-\Delta\alpha \cdot z) \tag{19}$$

$$\overline{Q(z)} = Q(z_\infty) \frac{O_{RR2}(z)}{O_{RR1}(z)} \tag{20}$$

252 where $R(z_\infty)$ and $Q(z_\infty)$ are the values observed when all overlap factors have become constant

253 at a sufficiently large range from the lidar, noted z_∞, after which variations of the optical path

254 inside the reception channels become negligible. $\Delta\alpha = \alpha(407\text{nm}) - \alpha(387\text{nm})$ is the difference

255 of atmospheric extinction between the two VR wavelengths.

256 To evaluate z_∞, we introduce in Figure 1 b) parameters that characterize the overlap of a paraxial

257 or coaxial lidar (e.g. Kuze et al., 1998): i) $z_e = 2e/\phi$ at which the emitted laser beam located at

258 distance e from the receiver axis enters the field of view, whose full size is ϕ; z_e is null for a

259 coaxial system ii) $H = D_{rec}/\phi$, the so-called hyperfocal distance, minimum range from which

260 the beam originating from a point still fully enters the field stop; iii) $H_{IF} = 2D_{rec}f/f'\theta'_{max}$, that

261 we might call the filter hyperfocal distance, similarly to the former, the minimum range from

262 which the image of a point does not exceed θ'_{max}, the AOI on the IF that significantly changes

263 its transmittance. z_∞ is above the maximum of those three, which is usually H_{IF}. If we use for

264 θ'_{max} the AOI value causing 1°C bias on temperature per Eq. (10) and Eq. (15), we find: $z_\infty > H_{IF}$

265 $= 780$ m. Note that z_∞ can reach several km with misaligned filters.

266 If for instance the lidar can be mounted on a rotating platform capable of aiming horizontally,

267 the overlap ratios $OR_R(z) = O_{H2O}(z)/O_{N2}(z)$ and $OR_Q(z) = O_{RR2}(z)/O_{RR1}(z)$ can be

268 estimated with suitable precision ($\sim 10^{-3}$) by averaging the signals over time and smoothing them

269 over range, and finally correcting for differential of extinction on the VR ratio:

$$\widehat{OR_R}(z) = \frac{R(z)}{R(z_\infty)}\exp(\Delta\alpha \cdot z) \qquad (21)$$

$$\widehat{OR_Q}(z) = \frac{Q(z)}{Q(z_\infty)} \qquad (22)$$

270 These estimates of the overlap ratios will then be used during signal processing for vertical

271 shots as in Eq. (4) and (5). However, assumptions are made for the former estimation, namely:

272 • As explained above, the atmosphere is assumed to be homogeneous in WVMR and

273   temperature (down to <0.5°C) up until z_∞, whereas the overlap ratios must be constant

274   (down to <0.4%) after z_∞. Also, the maximum range (with sufficient SNR) of the lidar

275   must exceed z_∞, implying nighttime measurements for the Raman channels. Therefore,

276   the effects generating overlap variation after a few hundred meters must be prevented.

277 • The lidar is assumed to retain the exact same overlap functions when aiming

278   horizontally and vertically. Considering a field of view around 1 mrad, the stability of

279   the emission and reception optical paths must be better than ~10 µrad between these

11

280   two positions. This is feasible for a small refractor but difficult for a Raman system such

281   as WALI, with a heavy laser and large reflector.

282 These difficulties make it extremely challenging to estimate the overlap ratios with an accuracy

283 better than a few percent. This is enough for the WVMR, but we find that a correction must be

284 applied by comparing with in-situ sounding for temperature measurements by Raman lidar.

285   3   Implementation and bias mitigation on the WALI system

286 In this section, we describe the WALI instrument from the emitter to the reception channels,

287 characterizing the critical elements in the framework of WVMR and temperature

288 measurements. The system has evolved from its previous implementation described in Totems

289 et al. (2019), by adding RR channels and a fibered telescope receiver. A global diagram

290 presenting the main lidar sub-systems is shown in Figure 2, and a summary of its characteristics

291 is given in Table 2.

292
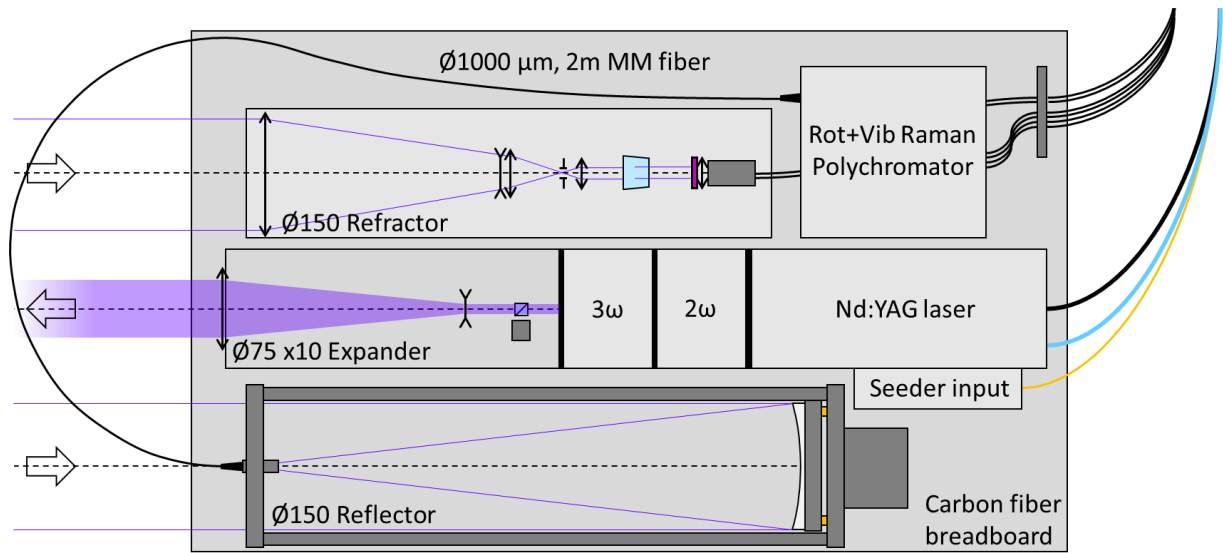
293 Figure 2. Global diagram of the lidar system. The main sub-systems are: the emitter (center),

294 the elastic receiver using a refractor (top), the Raman receiver using a fibered parabolic reflector

295 (bottom), and a separate, thermally stabilized polychromator (upper right). See Figure 5 for the

296 detail of the polychromator design.

297 Its main features are a single rotatable platform (lightweight carbon fiber breadboard by

298 CarbonVision GmbH) carrying both its emission and reception paths, a 150-mm refractor for

299 the elastic channels (for aerosol studies), and a 150-mm diameter parabolic fibered reflector for

300 all the Raman channels. The separation of the four Raman channels takes place in a deported

301 polychromator set in a thermally controlled enclosure, fed by the optical fiber. Fiber optics are

also known to partly scramble the input illumination, which could help minimize the range-dependance of filter transmittance or detector sensitivity for the different Raman channels. The output signals from the photomultiplier tubes (PMTs) in the polychromator are digitized by a NI^{TM} PXI system (not shown).

Table 2. WALI instrument characteristics summary (PRF: pulse repetition frequency, FOV: field of view, CWL: central wavelength in vacuum, FWHM: full width at half-maximum, OOB: out-of-band blocking specification, OD: optical density)

Emitter	Laser	Lumibird^{TM} Q-Smart 450 SLM, tripled Nd:YAG, frequency stabilized $\lambda_{laser} = 354.725$ nm in vacuum, $E_p = 100$ mJ, PRF = 20 Hz.
	Optics	High-power polarizing beamsplitter and 10x beam expander Output beam diameter: 65 mm, Em/Rec separation: 200 mm
Elastic receiver	Optics	Ø150 mm F/2 UV fused-silica refractor
	Spatial filter	0.67 x 2 mrad FOV
	Spectral filter	CWL = 354.71 nm, FWHM = 0.22 nm, OOB: OD >4.0
Raman receiver	Optics	Ø150 mm F/4 Newton reflector
	Spatial filter	Ø1.67 mrad FOV
	Fiber optics	Ø1 mm, 2-m long, OH-rich multimode fiber
	VR spectral filters	365 nm longpass (OD >2) + 395 nm (OD >2) beamsplitter + Materion^{TM} interference filters: N_2: CWL = 386.76 nm, FWHM = 0.27 nm, OOB: OD >4.0 H_2O: CWL = 407.59 nm, FWHM = 0.34 nm, OOB: OD >4.0
	RR spectral filters	365 nm shortpass (OD >2) + CWL = 355 nm, FWHM = 10 nm, flat-top, OOB: OD >6.0 + 50:50 non-polarizing beamsplitter + Materion^{TM} interference filters: RR1: CWL = 354.09 nm, FWHM = 0.24 nm, OD >6.0 at 354.7 nm RR2: CWL = 353.22 nm, FWHM = 0.54 nm
Detection	Photodetectors	Hamamatsu H10721-210 photomultiplier tubes (PMT) with >0.13 A/W cathode sensitivity
	Amplification	Up to $2\,10^6$. Elastic & RR: fixed, VR: sky-background piloted
	Acquisition	3x NI^{TM} PXI-5124 two-channel digitizers Sampling frequency: 200 MHz, 12-bit, Q-switch-triggered

| Recording | 1000 shots ($\Delta t_0 = 1$ min), 200 MHz ($\Delta z_0 = 0.75$ m) |
| | Analog + photon-counting |

3.1 Emitter

The emitter is a commercial Lumibird/Quantel "Q-Smart 450" Nd:YAG pulsed laser, stabilized by injecting the output of a single longitudinal mode fiber laser emitting at 1064.175 nm into the main cavity ("SLM" option), and frequency-tripled to emit at wavelength $\lambda_{laser} = 354.725$ nm (in vacuum). The nominal pulse energy for the Q-Smart 450 with SLM is 100 mJ at 355 nm, with a Pulse Repetition Frequency (PRF) of 20 Hz. These values set WALI near the eye safety limit for pulsed energy, making the system eyesafe at the output of a 2-meter funnel, as limited by leaks at 532 nm through the built-in filtering dichroic plates.

A critical issue to be cleared before using the Q-Smart 450 SLM in WALI was the spectral purity and stability of the laser, in terms of linewidth and wavelength drift. The laser seeder at 1064.175 nm is specified with a 50 MHz (0.062 pm at 355nm) stability at fixed temperature, and 37 MHz $^{\circ}C^{-1}$ (0.046 pm $^{\circ}C^{-1}$ at 355 nm) temperature drift.

Nevertheless, the stability of the Q-Smart emission at 354.725 nm has been verified with a dedicated optical setup, sending the output of a Michelson interferometer with optical path differences (OPD) between 0 and 100 mm on a UV-sensitive CCD camera. By extracting the contrast and phase variations of the fringes at large OPDs from the videos, we were able to ascertain:

- the laser linewidth, without seeder, to be 24±2 pm (versus 26.5 pm datasheet value), and with seeder, to be small compared to 1 pm (versus 0.2 pm datasheet value),

- the wavelength drift, without seeder, to be below 8 pm over 10 minutes, and with seeder, to be below 0.2 pm RMS (root mean square fluctuations) over 5 minutes. We consider the remaining fluctuations to be mostly due to the ~0.05 pm $^{\circ}C^{-1}$ temperature-linked drift of the seeder, which is not temperature-controlled and was recently turned on.

Given the requirements derived in Section 2.3, this makes the seeded Q-Smart laser theoretically suitable for RR measurements of temperature.

3.2 Raman receiver

In this sub-section we discuss the possible impact on the VR/RR ratios of the fibered reflector (beam scrambling and fiber optics fluorescence), of Raman filters characteristics, and of the

337 polychromator design and alignment. As far as we know, this type of comprehensive study does
338 not exist in the literature for Raman lidars.

3.2.1 Fibered reflector telescope and scrambling of the lidar field-of-view

340 The elastic and Raman receivers are both 150 mm in diameter. The focal length of the refractor
341 (elastic channels) is ~300 mm, which with a 200x600 μm field stop achieves full overlap at
342 ~150-200m. However, the focal length of the reflector (Raman channels) is 600 mm (parabolic
343 mirror with aperture F/4); this implies using a multimode fiber optics about 1 mm in diameter
344 as the field stop to allow similar results in terms of field-of-view and overlap. The chosen fiber
345 optics is an OH-rich UV fused silica fiber, 2 m in length and 1000 μm in core diameter, with
346 numerical aperture 0.22 (Avantes FC-UV1000-2).

347 Coupling the reflector output into a multimode fiber (e.g. Chourdakis et al., 2002) allows: i) to
348 minimize occultation of the primary mirror (here only 12 mm in diameter), ii) to deport the
349 Raman channel separation away from the telescope, making it a separately tunable optical
350 system, minimizing the overall lidar size and making light or temperature confinement easier,
351 iii) in theory, to scramble the fiber output illumination versus the lidar field angle, therefore
352 minimizing the range-dependence of AOIs on the IFs discussed in Section 2.3, and flattening
353 overlap ratios after the geometrical full-overlap distance.

354 The scrambling of the lidar field-of-view, via the multiple internal reflections in the fiber, has
355 been experimentally tested by imaging the output of the fiber, with a varying point-like input.
356 The results are shown in Figure 3. Note that the radial coordinate of the output point relative to
357 the center of the fiber corresponds to a given AOI on a well-aligned IF in the following
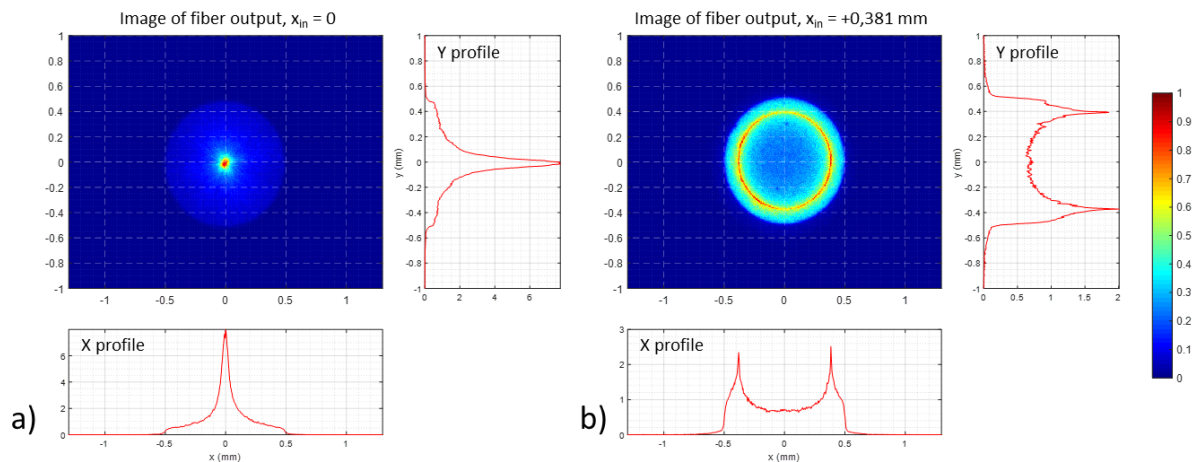358 polychromator, after a $f' = 50$ mm doublet lens.

359

Figure 3. Images of the output facet of the 1 mm diameter multimode fiber optics for a) centered and b) decentered (at $x_{in} = 0.38$ mm horizontal offset from the center of the core) input point of a 20-mm beam focused on the input facet of the fiber, and energy density profiles along the x and y axes.

It appears on Figure 3 b) that the input energy is mostly redistributed tangentially (i.e. along the angular polar coordinate, as opposed to radially) by its passage through the fiber. The radial dispersion remains small, and the mean output radius is approximately equal to the input radial coordinate. Manually applying curvature to the fiber, as suggested by so-called "mode scrambling" devices, did not make the energy distribution more uniform so much as creating unwanted losses (effect not shown). Even for a centered input, the energy radial distribution – i.e. the percentage of the total output in a given radial bin, that will therefore impact a well-aligned filter at the same AOI – is uniform. We conclude that even with the use of fiber optics the angle of incidence on the interference filters depends on the image positions in the focal plane of the telescope (i.e. mainly the distance to the optical axis), in contrast to what could be expected. Range-dependent biases will not be strongly mitigated.

3.2.2 Fiber optics fluorescence

It has been shown by Sherlock et al. (1999) and discussed by Whiteman et al. (2012) that fiber optics fluorescence could be an obstacle to water vapor measurements, because elastic scattering at 532 nm was inducing fluorescence in an OH-poor fiber at a non-negligible level compared to the atmospheric Raman scattering. It was solved by using an OH-rich fiber, but it was predicted in the latter work that the effect could be larger at 355 nm.

We have characterized this effect in the WALI fiber optics, using a narrowband CW laser excitation centered at 355 nm. The output of the fiber was analyzed by a Fourier transform spectrometer (Thorlabs OSA201C spectrum analyzer), behind a longpass dichroic plate cutting the direct laser emission, and the same collimating achromat as in the polychromator. The resulting spectrum is shown in Figure 4.

We plot both the raw spectrum and the Fourier transform spectrometer noise floor after 1000 profile integrations, to highlight the very weak features observed at 780 to 910 nm, and the high associated uncertainty. Due to the noise level, and given the dichroic plate residual transmittance of the laser wavelength, we can only ascertain that the fluorescence power spectral density (PSD) around 400 nm is lower than 10^{-6} times the peak laser PSD, although no feature can be detected in this spectral domain. Note that fluorescence between 400 and 500 nm was indeed observed using a broadband excitation from a fibered LED at 340 nm (not shown).

16

393 Nevertheless, the amount of rejection observed for a 355 nm excitation is sufficient to exclude
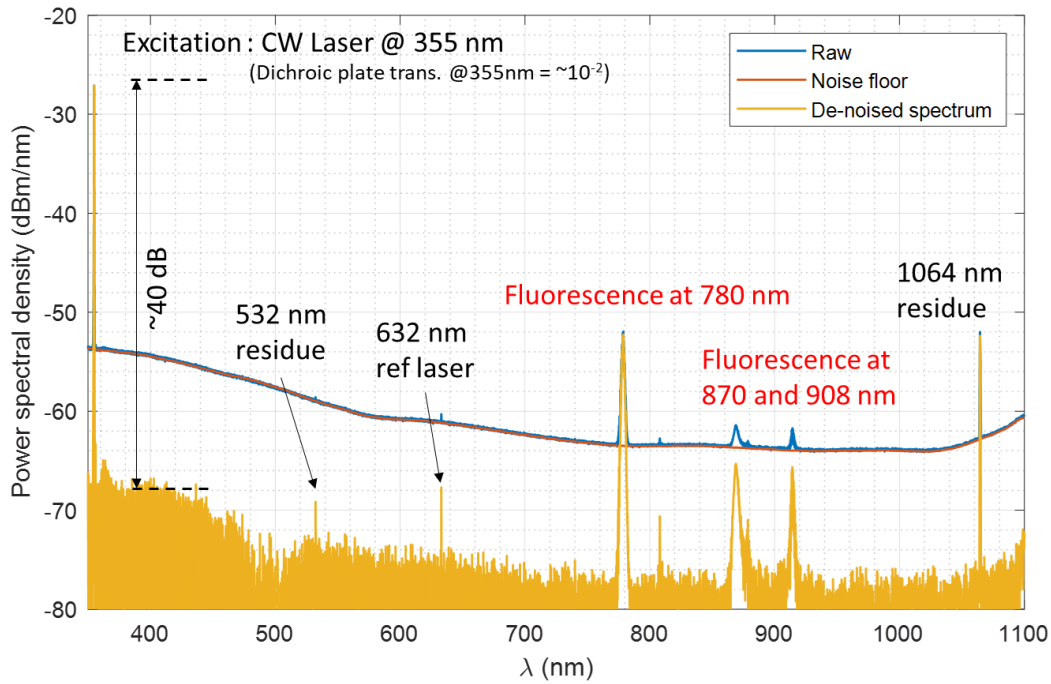394 an adverse impact of the OH-rich fiber optics for Raman lidar measurements.

395

397 Figure 4. 1000-µm diameter, 2-meter long fiber fluorescence measurement with 355 nm laser
398 illumination.

399 **3.3 Raman channels**

400 3.3.1 Polychromator configuration

401 The RR+VR polychromator configuration used in WALI is presented in Figure 5. Dichroic and
402 non-polarizing beamsplitters are used to separate the channels. In contrast to the design of
403 Hammann et al. (2015) which optimizes throughput and laser-line rejection on the RR channels,
404 we chose to implement a splitter-based configuration, favouring a compact system (25x25 cm,
405 easier to confine) and normal incidence on the filter, at the expense of SNR. Indeed, designing
406 the filters for a correct CWL at 5° incidence (as in the cited work) instead of 0° dramatically
407 narrows the filter angular acceptance, as can be deduced by deriving Eq. (15) as a function of
408 incidence θ'. In the WALI polychromator, the output from the fiber is collimated by a near-UV
409 achromat with 50 mm focal length, resulting in a 22 mm diameter beam. Dichroic beamsplitters
410 with adequate cut-on wavelengths are used to separate channels. On each separated channel, an
411 aspheric lense condenses light on the PMT surface, located 4 mm before the focal plane. A steel

17

cage system assembly holds all parts with great stability, however beamsplitters are not always
perfectly aligned at 45° in the stock cage cubes. That is why all filter, lens and PMT sub-
assemblies are mounted on tiltable mounts to allow precise alignment at normal incidence.
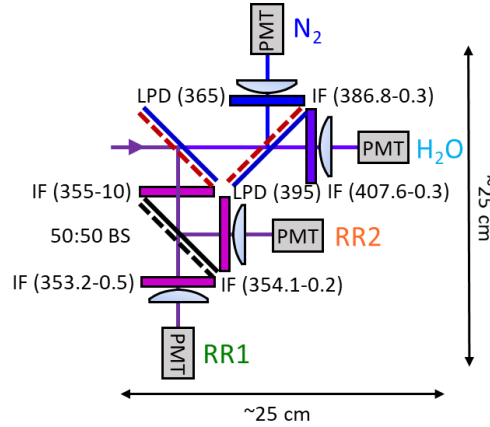

Figure 5. Compact rotational & vibrational Raman separation configuration used in WALI. IF: interference filter (with CWL - FWHM given in nm), BS: beam splitter, LPD: long-pass dichroic beamsplitter (with cut-off wavelength given in nm), PMT: photo-multiplier tube. This polychromator is thermally regulated in a dedicated light-tight enclosure.

3.3.2 Filters qualification

All interference filters were custom-made by Materion, including the RR filters on specifications graciously shared by the team of A. Behrendt (following Hamann et al., 2015). They were characterized on the Fourier transform spectrometer (described in section 3.2.2) prior to mounting, using fibered LEDs peaking at 340, 385 and 405 nm as the light source; the beam was collimated by the same near-UV achromat with 50 mm focal length. We give the measurements results for the RR filters in Figure 6 and Table 3.

The effective index and angular acceptance of the filters (arbitrarily chosen for a 10% loss at the CWL) were assessed by tilting the filters of a known angle. A critical parameter, the transmittance of both filters at the laser line λ_{laser} in operational conditions was assessed on the lidar itself, by measuring the energy of an echo on a hard target located at 200 m, and switching between an elastic IF of known transmittance with a known strong optical density and the RR IF in question. The excellent extinction in the RR1 filter guarantees a minimal effect of elastic signal leak in temperature retrievals, but it was nevertheless subtracted as in Eq. (3). Note that no significant echo was detected on the H_2O-Raman channel, indicating extinction better than a few 10^{-9}, thanks to the two dichroic plates.
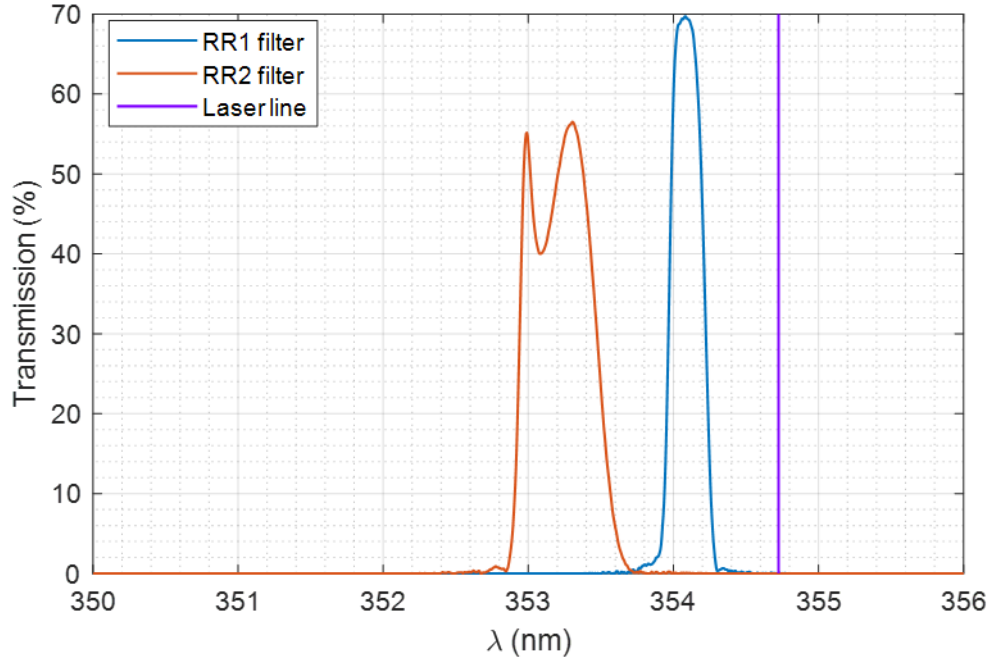
436

Figure 6. RR filters spectral transmittance measured on optical spectrum analyzer with illumination by a 340 nm LED: RR1 (low-J) and RR2 (high-J) filter at 0° incidence.

Table 3. Measured RR IF characteristics. All CWL values are given in vacuum.

	RR1 filter	RR2 filter	Uncertainty
CWL	354.09 nm	353.22 nm	0.01 nm
FWHM	0.24 nm	0.54 nm	0.01 nm
n_{eff}	1.62	2.03	0.05
Max transmittance	69%	51%	5%
Laser line transmittance	$2.7 \ 10^{-8}$	$2.9 \ 10^{-7}$	10% relative
Angular acceptance (AOI for 10% loss at CWL)	1.5°	2.5°	0.2°
CWL shift at max field angle (i.e. edge of fiber, AOI = 0.59°)	-9.8 pm	-2.5 pm	0.3 pm

3.3.3 Polychromator alignment and qualification

Due to the filter CWL shift evolving as the square of the AOI in Eq. (15), it is essential to minimize range-dependent biases by aligning the filters at a precisely normal incidence from the input beam. However off-the-shelf beam splitter plate holders are found to be misaligned

19

by up to 1° from an ideal 45° incidence. All PMTs are mounted jointly with their own IF and lens into a tiltable mount to correct for this (represented on Figure 7).

The alignment of these mounts is performed in the lab by conjugating an input multimode fiber of 600 μm diameter replacing the lidar input, into a target fiber 200 μm in diameter at the focus of the PMT lens, through the polychromator. Fibered LEDs are used for illumination like in section 3.3.2. All the channels are sequentially addressed in this manner. By obtaining a maximal energy and a radially uniform profile at the output of the target fiber, one can ensure alignment with a precision of 0.1 to 0.3°.
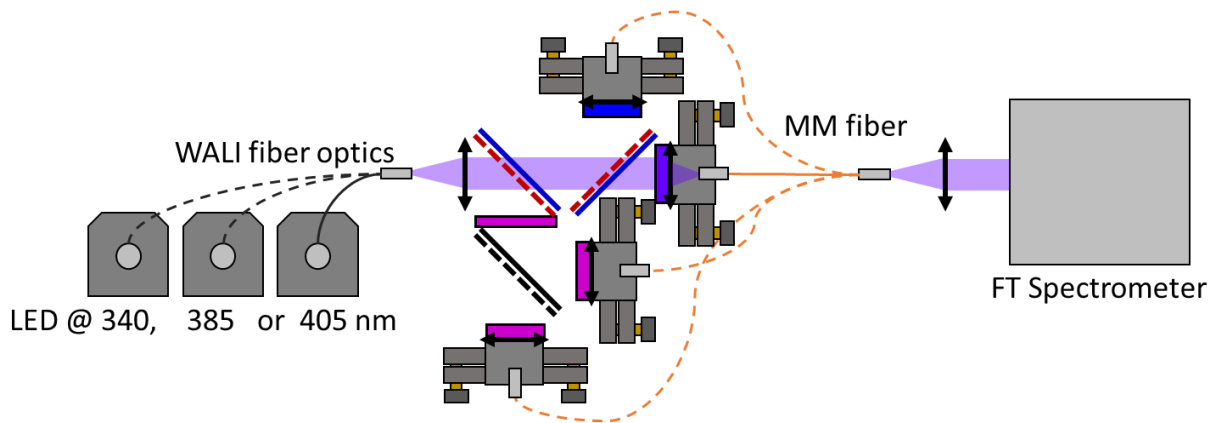
Figure 7. Method for polychromator alignment validation. Light from LEDs is input in the WALI fiber optics, passes through the polychromator, and into a multi-mode fiber (MM fiber, Ø600 μm) analysed by a Thorlabs OSA201C Fourier transform spectrometer. Channel central wavelengths are expected not deviate from those of the filter measured independently at normal incidence, to validate alignment.

To verify the result, the spectral transmittance of the polychromator channels themselves are characterized by the Fourier transform spectrometer, as shown on Figure 7. By illuminating the channel with a LED coupled in the actual lidar fiber, we ensure that the polychromator is studied in operational conditions. The CWL of each channel is expected not deviate by more than 20 pm (twice the empirical accuracy) from the CWL measured on the individual filter at normal incidence, to validate the alignment. The polychromator aligned using the procedure proposed above passes this test.

3.4 Detectors

Hamamatsu 10721P-210 PMTs, with >0.13 A W^{-1} cathode sensitivity at 400 nm, and up to ~2 10^6 controllable internal gain, are used to transform the optical flux into an electric current, directly digitized at 200 MHz (0.75 m sampling along the line of sight) by three NI PXI-5124

469   two-channel digitizers with 50 Ω load. The acquisition software, custom-made with Labview,

470   conducts analog and photon-counting (thresholding at ~3 standard deviations of the noise)

471   accumulations in parallel during 1000 shots (50 seconds), every minute, which are then pre-

472   processed and recorded (~10 seconds down time). Every ~8 minutes, baselines are recorded

473   with PMT gains set at zero. The next sub-sections describe critical points of the detectors

474   affecting the RR and VR channel ratios.

3.4.1 PMT response variability

476   As explained in Section 2.3, the non-uniformity of the PMT response can affect the ratios of

477   Raman channels as a function of range. We tested the sensitivity profiles of WALI's H_2O-

478   Raman PMT to continuous laser illumination at 405 nm wavelength, first using a 1-mm

479   diameter collimated beam, as a function of both point and angle of incidence. A cumulated ~6.0

480   neutral density filter was used to avoid saturation of the PMT.

481   As shown on Figure 8 a), a strong variation of sensitivity by a factor of almost 2 is found on the

482   PMT surface, much larger than specified. The relative sensitivity is lowest near the center of

483   the PMT and highest on the sides, on a diameter of 4 mm approximately equal to the spot size

484   in the lidar. Indeed the PMT surface is 4 mm before the focal plane of the 0.5 NA condensing

485   aspheric lens. This is consistent with the results of Simeonov et al. (1999) on an older generation

486   of detectors, excluding a suspected hole-burning phenomenon over the lifetime of our PMT.

487   On the vertical axis, we also note the effect of the gridded cathode. Note that sensitivity does

488   not vary by more than a few percent as a function of angle of incidence (not shown).
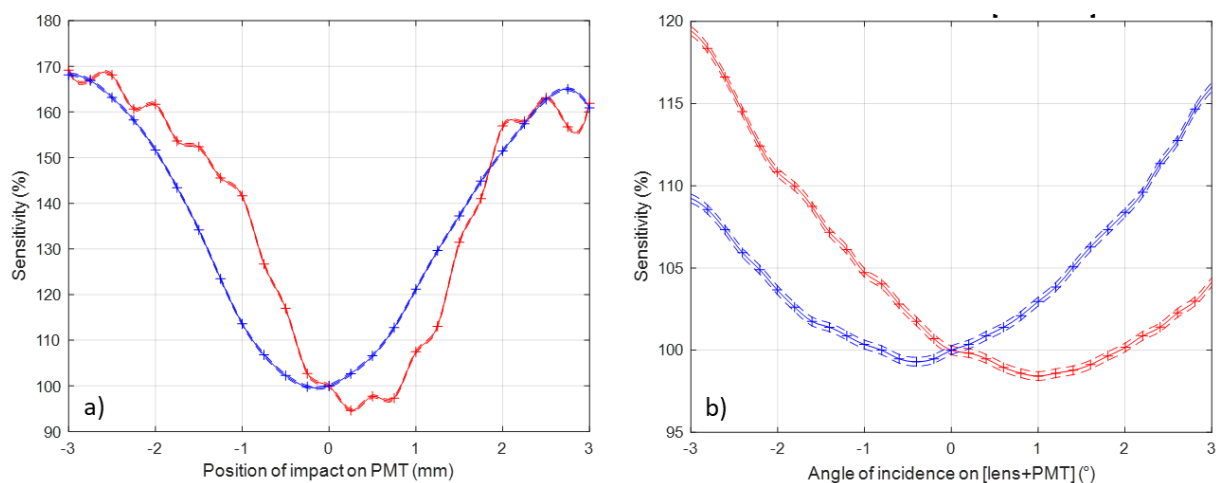

490 Figure 8. Study of the non-uniformity of the PMT response: a) as a function of point of impact
491 on the active area along the horizontal (blue) and vertical (red), with a 1 mm collimated beam
492 from a 405 nm laser, b) as a function of angle of incidence on the lens and PMT assembly
493 similar to the ones used in the WALI polychromator, with a 22 mm collimated beam from the

21

same laser. Dashed lines represent uncertainty calculated over multiple measurements. Sensitivity is given normalized by its value at the approximate mechanical centre of the PMT or at normal incidence as determined using the reflection on the attached neutral density filter.

We then put the condensing lens used in the polychromator in front of the PMT, and studied its response as a function of AOI on the lens+PMT assembly, which is shown in Figure 8 b). The input beam was the nominal size in the polychromator ie. ~22 mm in diameter. We find that the curve corresponds well to the measured sensitivity profile, smoothed by its convolution with the spot on the PMT. The problem is that at normal incidence, the derivative of sensitivity with incidence is 2-5% per degree. Using the calculations in Section 2, a $\theta = 1$ mrad field angle corresponds to 0.39° incidence on the PMT, inducing potentially 0.8-2% bias on R and Q, and thus a significant 1 to 2°C bias on temperature. In the future, the condensing lenses will be replaced with afocal beam reducers to reduce this dependency.

3.4.2 Baseline and EM parasites correction

The baseline induced by the detection chain is found to vary between channels and in time. It is also subject to electro-magnetic (EM) interference causing parasitic signals of both high frequency, mostly due to the flashlamp high peak current radiating over the system, and low frequency, probably due to other neighboring electronics. For this reason, the channel baselines are evaluated regularly (by averaging 1000 shots with PMT gain set to zero, every 8 minutes), smoothed and corrected (L_j in Eq. (2)). However, for the Raman channels (H_2O and RR2 specifically), the weakness of the signals requires a specific care of EM compatibility, as repeating parasitic spikes were found to jam the channels (especially photon counting which relies on thresholding) starting at altitude 6-7 km.

Figure 9 a) shows an example of perturbed baseline. Trial and error established that common methods to avoid ground loops were not all efficient: star grounding of the various cables worsened the problem, whereas physically separating coaxial signal cables from direct current power supply and control voltage cables, and grounding all connectors and opto-mechanics again on the breadboard side, mitigated it, reaching the baseline plotted in Figure 9 b). Note that baseline variation is not significant between successive evaluations without an external perturbation; the estimated baseline is automatically subtracted from the profiles before recording during the next 8 minutes (Eq. (3)).
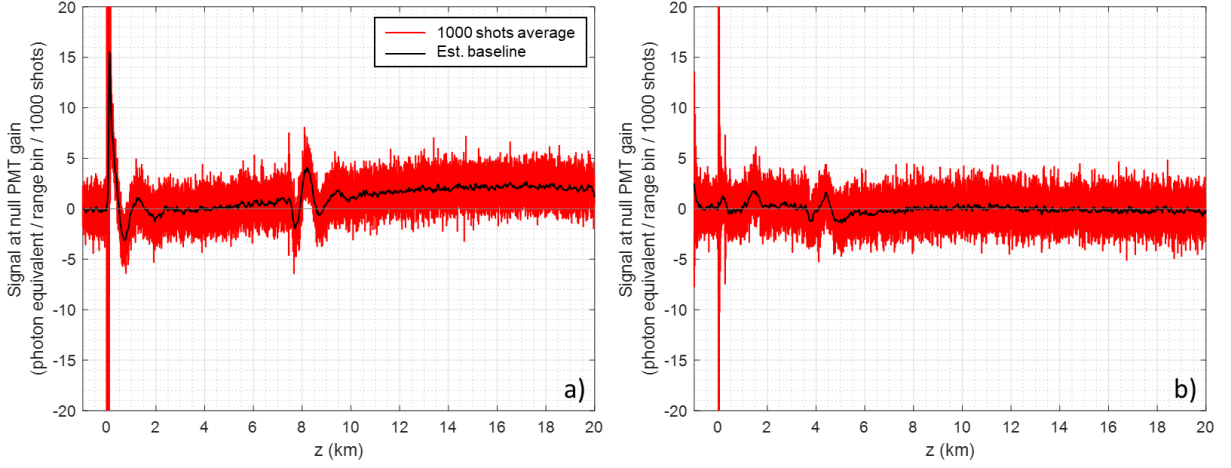
Figure 9. Analog detection baseline measurements (red) over 1000 laser shots with PMT gains set to zero, expressed in photon counts equivalent on the RR2 channel: a) in an unfavorable case (no mitigation), showing both baseline fluctuations over time (20 km ~ 133 µs) and strong electro-magnetic parasites at large distance; b) on the WALI system, after mitigation. The final estimated baseline ($\hat{L}_j(z)$ in Eq. (3)) obtained after smoothing, which is subtracted to all recorded profiles, is in black.

3.4.3 PMT gain adaptation

On each channel, PMT internal amplification gain G (using photoelectron multiplication) is a definite function of its control voltage U. The variation of G by ~2 orders of magnitude allows for the optimization of the dynamic range. This helps deal with the different Raman cross-sections in each filter, with variations of atmospheric transmittance, and especially with sky background levels during daytime. The gain is pushed at its maximum possible value still satisfying two conditions: i) the signal voltage maximum does not exceed the range of the digitizer, ii) the sky background signal does not exceed the maximum output current of the PMT that guarantees linearity (100 µA, ie. $<S_{raw}> < 5$ mV). This is indispensable for day-round measurements of WVMR, otherwise the channels would be saturated during daytime (Chazette et al., 2014b), or suboptimal in SNR during nighttime.

However, PMT gain adaptation leads to biases on the Raman channel ratios if the gain versus control voltage characteristics are not known with a better precision than the requirements stated in Table 1 (2% on VR channels, 0.4% on RR channels). In Figure 10 a), we show the experimental calibration of G versus U as well as second-degree polynomial fits for each channel. The relative error on the VR and RR channel gain ratios approximated by these models is plotted on Figure 10 b), with the measurement uncertainty. This uncertainty is mostly due to

23

548   variations of atmospheric parameters and laser energy during calibration. Since all relative

549   errors are well centered, we compute that the possible error for the gain ratio with these models

550   is ~1.3 %. This is compatible with WVMR measurements but not with temperature

551   measurements. Therefore, the PMT gain should only be adapted on the VR channels, and the
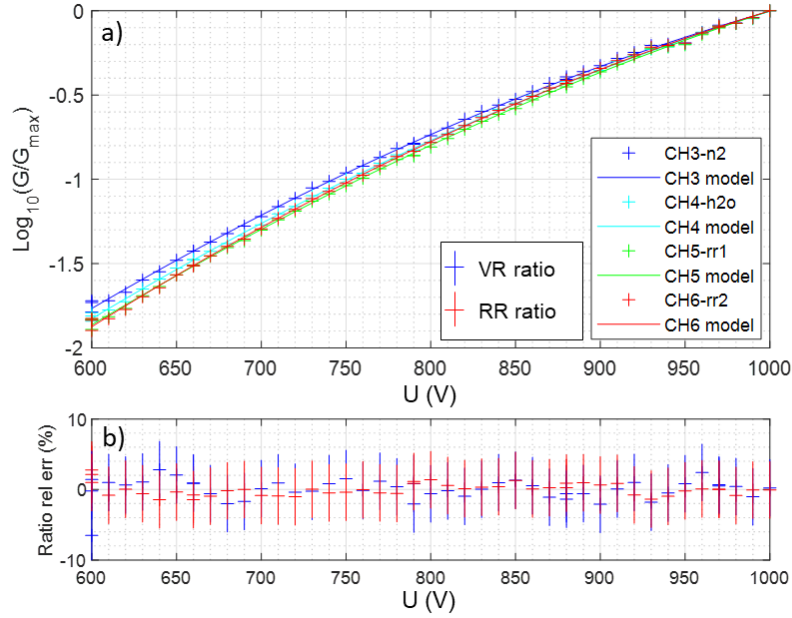
552   RR channels should be kept at a fix value of gain.

553

554   Figure 10. Calibration of PMT gain G versus control voltage U: a) log-gain measurements and

555   second-degree polynomial model for all Raman channels, and b) relative gain ratio error

556   between model and measurements for vibrational and rotational Raman channel ratios.

557   ### 3.4.4 Merging analog and photon-counting signals

558   Both analog and photon-counting raw signals are recorded. The analog signal has lesser SNR

559   at high altitude during nighttime, whereas the photon-counting signal is saturated at low altitude

560   and by daylight; by merging them correctly, an optimal SNR can be obtained (Newsom et al.,

561   2009). For signal processing, the photon-counting raw signals are first desaturated (details in

562   Chazette et al., 2014b). Merging is performed during nighttime on the pre-processed signals

563   defined in Eq. (3). After calculating a photon to Volts conversion constant at an altitude where

564   photon-counting is not saturated, the converted photon-counting profile replaces the analog

565   profile after a predefined altitude depending on signal strength (from 1 km for the H_2O VR

566   channel, up to 4 km for the elastic channel).

567   We wish to emphasize here that baselines L_j and background signals B_j in Eq. (3) must be

568   estimated separately for the analog and photon-counting recorded profiles (which have no

569 baseline, and a smaller but non-zero background value due to the suppression of electronic

570 noise). Otherwise, the merged signal will show discontinuities at the cut-off altitude, and biases

571 at high altitude at dusk and dawn. Their impacts are typically much larger than the requirements

572 of Section 2.2.

4   Qualification on the atmosphere

574 In this section, we qualify the WALI system starting with the measurement of its overlap factor

575 ratios, followed by its calibration and comparisons with radiosoundings. Remaining biases are

576 highlighted and corrected, and experimental measurement errors are evaluated.

4.1   Experimental set-up and strategy

578 We put the lidar into operation in our laboratory near Saclay (48°42'42"N 2°08'54"E) over a

579 period of two weeks in May 2020. It was placed on a rotating platform below a trapdoor

580 equipped with silica windows for zenith shots, and in front of a window at a height of about 9

581 m above the ground level (agl) for horizontal shots. During the latter, the lidar aimed North <5°

582 above the horizon (beam elevation <80 m per km of range). In that direction, land use is fields

583 up to 800 m range, buildings and trees between 800 and 2 km range, and fields again up to 5.5

584 km range.

585 To calibrate and qualify the lidar measurements, we use radiosoundings launched two to three

586 times daily from the operational Météo-France station located in Trappes (48°46'27"N

587 2°00'35"E), 12.3 km WNW from the lidar near Saclay, approximately upstream in the

588 prevailing winds, although the wind was oriented mostly NE during the May 2020 period.

4.2   Measurement of overlap ratios with horizontal shots

590 The overlap factors and their ratios were estimated on signals averaged over 3 hours after sunset

591 on December 19th, 2019, with a tepid (14°C), non-turbulent but hazy atmosphere (aerosol

592 extinction coefficient 0.32 km^{-1} at 355 nm with Angström exponent ~1.5, 11°C ground

593 temperature, and WVMR at ground level around 6.5 g kg^{-1}). With a planetary boundary layer

594 (PBL) height of ~900 to 1000 m, and slow gradients of temperature (−1 to −4°C km^{-1}) and

595 WVMR (−0.8 to −1.2 g kg^{-1} km^{-1}) in that PBL (as measured by radiosoundings launched from

596 Trappes at ~12:00UTC and 0:00UTC, presented in the next subsection), conditions were

597 excellent for a homogeneous atmosphere within the first 5 km at least.

The estimated overlap factors of the different channels, with atmospheric extinction fitted between 800 and 2000 m, are shown in Figure 11 a). Full geometrical overlap is obtained as expected between 150 and 200 m, but the curves differ by several percent between the Raman channels. Atmospheric extinction drifts from the estimated value after 2 km.

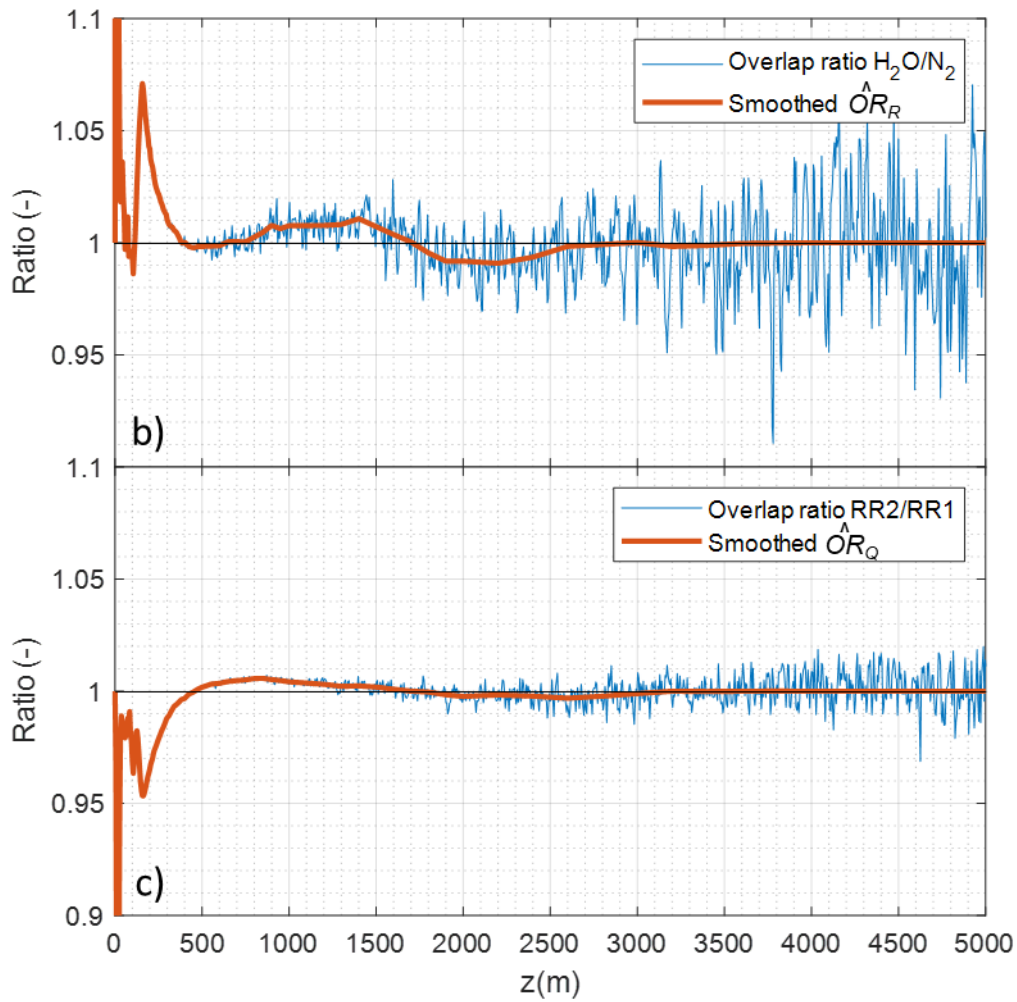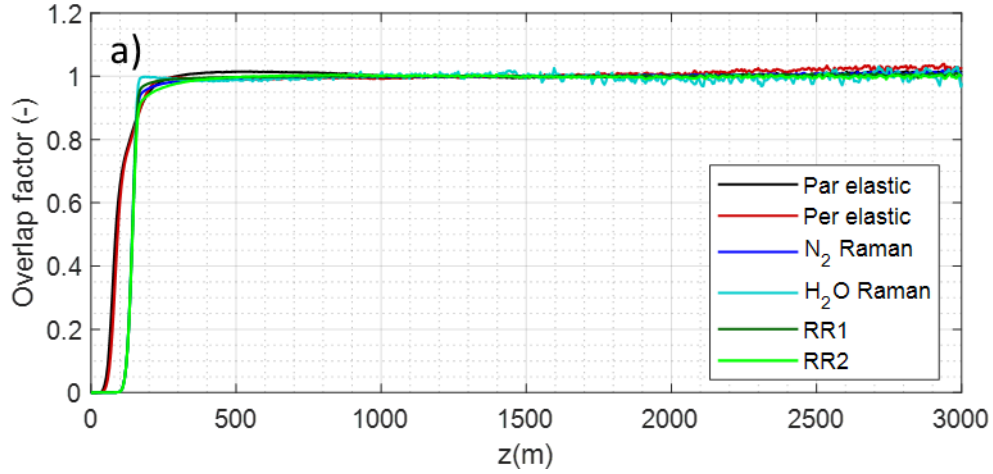Figure 11. a) Overlap factors measured over 3 hours of nighttime measurements with a horizontal line-of-sight on Dec. 19, 2019. Estimated overlap ratios between VR (b) and RR (c) channels: native resolution (thin blue line), final estimate after smoothing (thick red line).

The estimated ratios of overlap factors OR_R and OR_Q are plotted in Figure 11 b) and c), at 7.5 m resolution (thin line) and after smoothing (thick line, final correction used hereafter). Peak divergence is 5 to 7 %, at ~150 m. Convergence within 1% happens at ~400 m, but oscillations of lower amplitude persist until ~3 km. We note that for OR_Q, deviations do not exceed the ±0.7% required to maintain bias below 1°C. They are nevertheless corrected.

4.3 Comparison to radiosoundings and calibration, estimation of residual error

12 nighttime and 24 daytime radiosoundings were launched from Trappes between May 20th and June 2nd, 2020. Lidar profiles are averaged from 0 to 40 minutes after the radiosounding launch time. The range averaging is progressive and defined to keep the night time temperature error below 1.5°C: range bins are 15 m long below 100 m agl, growing to 360 m above 8 km agl.

In order to debias WVMR and temperature measurements from residual errors on OR_R and OR_Q, we perform a three-step calibration:

- First step: we exclude the first 1500 m agl of the profiles when fitting r_{H2O} *in-situ* vs R' and Q' vs T *in-situ* to estimate K and f respectively. This initial calibration is shown in Figure 12 a) & d).

- Second step: using these first estimates, we then plot the ratios between the lidar observables R' & Q' and the expected observables deduced from the in-situ measurements and these initial calibration parameters. This provides an estimate of the remaining biases on OR_R and OR_Q, which we find to be up to ~4% and ~1.8% respectively. This represents a small correction to the overlap ratios estimated while shooting horizontally, but remains larger than the requirements of precision specified in Table 1. The modelled corrections of OR_R and OR_Q are plotted in red in Figure 12 b) & e). We fit a sum of three exponential falls to the mean, of the form: $1 + a_1 \exp(-z/z_1) + a_2 \exp(-z/z_2) + a_3 \exp(-z/z_3)$, with a_i coefficients and z_i ranges to be adjusted.

- Third step: we apply the previous estimates of OR_R and OR_Q and we perform a new calibration using all the data (down to 200 m agl), yielding more precise estimates of calibration constants, as shown in Figure 12 c) & f).

635 In the three steps, data with SNR lower than 10 for R' and 30 for Q' are rejected so as to
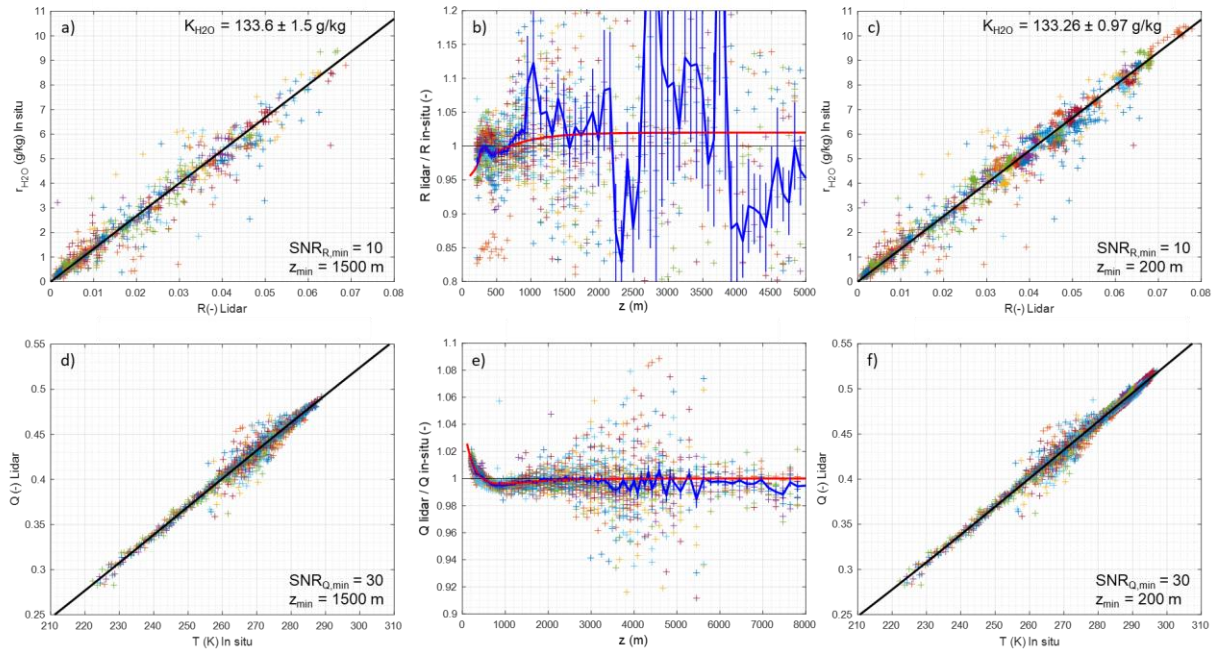636 limit the impact of noise present at higher altitudes.

638 Figure 12. Results of calibration on 12 nighttime and 24 daytime radiosoundings launched from
639 Trappes between May 20th and June 2nd, 2020 for WVMR (upper row) and temperature (lower
640 row), in three steps: calibration on measurements above 1500 m (a/d) with samples as crosses
641 (one color per radiosonde) and calibration curve in black; residual overlap ratio estimation (b/e)
642 with samples as crosses, mean ratio in blue, random error on mean ratio as vertical bars, and
643 model in red; calibration on all results (c/f). Daytime samples are limited to SNRs above 10 for
644 R' (WVMR) and 30 for Q' (temperature).

645 The reliability of this calibration along time has been tested by comparing to the same exercise
646 performed two months later at the end of July 2020. After calibration in the same conditions
647 than in May, we found K decreased by ~7.3%, and the temperature associated to a given value
648 of Q' to be ~2.1°C higher. However, OR_R and OR_Q were still accurate within the reachable
649 precision, ie. ~0.2%. It was later proven that a malfunction of the laser seeder was responsible
650 for a slow drift of the emitted wavelength. Thus, although a regular verification of the
651 calibration is necessary, the measurement of the overlap ratios is reliable.
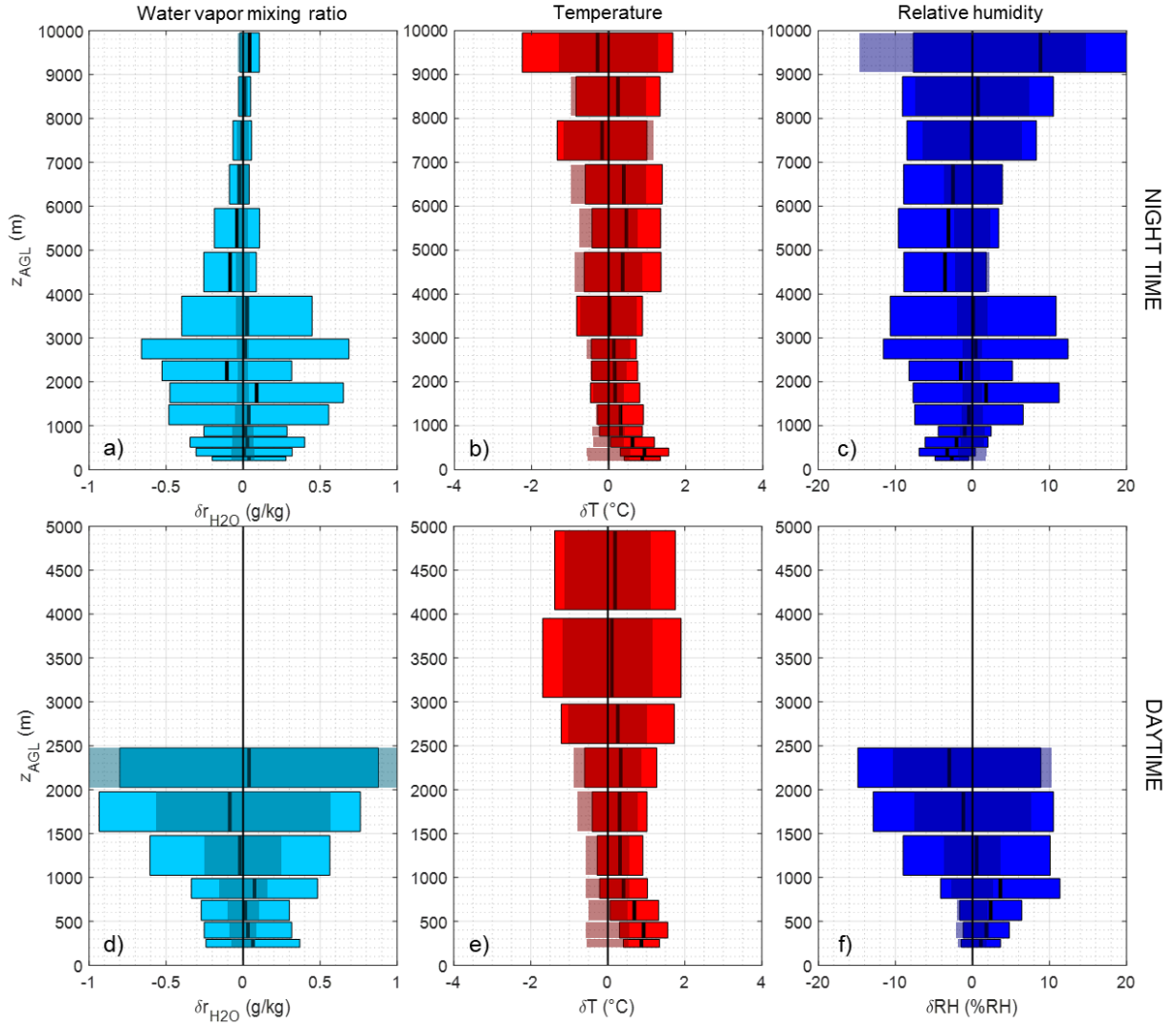
Figure 13. Residual deviations between lidar and Trappes radiosoundings in terms of WVMR, temperature and relative humidity, for night time (a/b/c) and daytime (d/e/f), with mean deviation (thick lines), and RMS error (colored rectangles). The error corresponding to noise levels on the lidar signal is shown as darker rectangles. Cloudy profiles have been discarded. Daytime measurements are limited to SNRs above 5 for R (WVMR) and 20 for Q (temperature).

In Figure 13, we examine the residual deviations between the lidar and the same series of radiosoundings used for the calibration. RH has been derived using Eq. (14) from lidar-estimated WVMR and temperature, and the pressure profile given by radiosoundings. For each parameter r_{H2O}, T and RH, we plot for daytime and night time profiles the mean and RMS deviations averaged over large range bins as colored bars, as well as the propagated signal error as darker shaded areas. This allows to compare the observed random error to what could be expected from the level of noise on the lidar measurements. Note that only profiles with good SNR unperturbed by clouds have been selected for this comparison.

666 On WVMR, the results show little bias, and RMS deviation is dominated by spatial atmospheric

667 variability at night and at low altitude (when SNR is high), and by lidar noise in all other cases.

668 On temperature, most of the RMS deviation is explained by noise; a ~1°C significant bias is

669 still seen below 800 m. This could be due in part to an underestimated correction of ORQ (only

670 ~0.8%) due to the regularized model used to approximate it, but also to local effects. On Figure

671 13 c) and f) are plotted the consequences of this bias on relative humidity *RH* to be around 2 to

672 4%RH, but also the resulting error to be expected. We see that with the defined averaging,

673 random error is around 2% RH up to 5 km agl during nighttime and 1 km agl during daytime,

674 growing fast above.

675 Table 4. Statistics of observed differences for r_{H2O}, *T*, and *RH*: experimental Mean Differences

676 (MD), Root-Mean Square Differences (RMSD), averaged over two different range bins, in the

677 low troposphere (1-2 km) and the free troposphere (5-6 km). Comparison to the "natural"

678 atmospheric variability between the lidar and RS sites as modelled by the ECMWF/IFS ERA5

679 reanalyses (difference over the considered period between grid points nearest to each of the two

680 sites), and to the theoretical root-mean-square error (RMSE) derived from the variance of the

681 RR signals. The grid points are located 8 km WNW of the lidar and 2 km S of the RS launching

682 station respectively, 18.3 km apart, and almost all RS trajectories below 6 km altitude are

683 contained within the same "pixel" of the ERA5 fields as the RS station.

	Range	Range resolution Δz	Model atmos. MD	Experimental MD (night/day)	Model atmos. RMSD	Theo. RMSE (night/day)	Experimental RMSD (night/day)
WVMR (g/kg)	1-2 km	84 m	-0.03	+0.06/-0.05	0.41	0.03/0.4	0.54/0.65
	5-6 km	168 m	$<10^{-2}$	-0.07	0.11	0.04	0.15
Temperature (°C)	1-2 km	84 m	+0.15	+0.25/+0.3	0.33	0.4/0.7	0.6/0.7
	5-6 km	168 m	+0.05	+0.4	0.28	0.75	0.95
Relative humidity (%RH)	1-2 km	84 m	-0.23	+0.8/-0.5	6.37	1.7/5.5	6.5/10
	5-6 km	168 m	-0.70	-3.3	7.52	2.2	7

684

685 To support the above interpretation, in Table 4 we compare the experimental mean difference

686 and RMS difference plotted on Figure 13, averaged over two altitude ranges (low troposphere,

687 LT, 1 to 2 km, and free troposphere, FT, 5 to 6 km), to i) the natural variability of the atmosphere
688 between the radiosondes at Trappes and the lidar at LSCE, as modelled by ERA5 reanalyses of
689 the ECMWF/IFS weather model, ii) the expected random error given the noise level on the RR
690 signals. Nighttime and daytime values are indicated in the LT, only nighttime values in the FT.

691 We see that the experimentally observed values of RMSD are rather consistent with the
692 quadratic sum of the RMS variability of the atmospheric variables between Trappes and LSCE,
693 and of the noise-induced RMS error. The excess random difference is thus well explained by
694 the distance. There is still a discrepancy with the mean difference of temperature however; it is
695 not fully explained by the differences of temperature at the locations of the two profiles seen in
696 ERA5. The model used to approximate the correction may be imperfect, and introduce small
697 errors when the necessary correction is large and fast-varying. We aim to improve this in the
698 future by a better estimation the overlap ratios horizontally, for instance using a large folding
699 mirror instead of tilting the lidar, which induces varying mechanical constraints on the optics.
700 This should greatly reduce the necessary correction function and the remaining error should be
701 limited by the horizontal inhomogeneity of the atmospheric temperature over a few kilometers.

5 Conclusion

703 During the qualification of the rotational Raman channels for the WALI lidar of LSCE, with
704 the aim of providing profiles of relative humidity, we encountered important sources of bias
705 that are seldom described in the now abundant literature involving such systems. We
706 highlighted the predominant effects of the dependency of filter transmittance and detector
707 sensitivity upon angle of incidence and point of impact, respectively. Because the latter
708 parameters are directly proportional to field angle, they cause range-dependent biases on the
709 RR/VR signal ratios that are several times greater than the required accuracy of lidars for
710 temperature measurements (only 0.79% for 1°C here), less so for water vapor measurements.
711 We established that this effect cannot be suppressed by using fiber optics between the receiver
712 and polychromator, because scrambling of the lidar field of view does not happen radially in
713 the fiber. Mitigation efforts impose the careful alignment of each filter at normal incidence to
714 the input beam, and the verification of the spectral transmittance of each channel on a
715 spectrometer. The thermal stability of the polychromator is also of prime importance. Other
716 significant bias sources include electro-magnetic perturbations of signal baselines and PMT
717 gain variation, which must be mitigated. The impact of fiber optics fluorescence, and of the
718 measured laser linewidth or short-term wavelength drift were shown to be negligible in the
719 WALI system.

After a measurement of RR/VR channel ratios during horizontal shots, which showed the significant impact of the above phenomena (up to 5% bias on ratios below 300m, ~1% higher), we calibrated and de-biased the WALI measurements using radiosondes launched from the nearby Trappes station of Météo-France. Between the de-clouded lidar measurements and the radiosonde profiles, the remaining mean differences are small (below 0.1 g/kg on water vapor, 1°C on temperature) and RMS differences are consistent with the expected error from lidar noise, calibration uncertainty, and horizontal inhomogeneities of the fields between the lidar and radiosondes. On relative humidity we thus reach a goal of ~10%RH random error and 5%RH systematic error up to 9 km by night and 1.5 km by day, with 40 min time integration and progressive vertical integration of 15 to 360 m at 10 km. The systematic error on RH is dominated by bias on temperature, whereas the random error is dominated by noise on water vapor measurements.

Thus exhaustively qualified, the WALI system may be applied in the near future to exercises assimilating thermodynamic profiles in weather models, as is expected within the WaLiNeAs (Water vapor Lidar Network Assimilation experiment) project (Flamant et al., 2021). The long-term temporal evolution of Raman channel calibration, expected from various effects like differential PMT aging or laser seeder drift, induces biases variable in time over the time-scale of such a project (several months). This aspect is becoming a main focus as the community works towards operational uses of weather Raman lidars (eg. Hicks-Jalali et al., 2020).

References

Adam, S., Behrendt, A., Schwitalla, T., Hammann, E. and Wulfmeyer, V.: First assimilation of temperature lidar data into an NWP model: impact on the simulation of the temperature field, inversion strength and PBL depth, Q. J. R. Meteorol. Soc., 142(700), 2882–2896, doi:10.1002/qj.2875, 2016.

Behrendt, A.: Temperature Measurements with Lidar, in Lidar: Range-Resolved Optical Remote Sensing of the Atmosphere, vol. 102, edited by C. Weitkamp, pp. 273–306, Springer-Verlag, New York., 2005.

Behrendt, A. and Reichardt, J.: Atmospheric temperature profiling in the presence of clouds with a pure rotational Raman lidar by use of an interference-filter-based polychromator, Appl. Opt., 39(9), 1372, doi:10.1364/AO.39.001372, 2000.

Behrendt, A., Wulfmeyer, V., Hammann, E., Muppa, S. K. and Pal, S.: Profiles of second- to fourth-order moments of turbulent temperature fluctuations in the convective boundary layer: first measurements with rotational Raman lidar, Atmos. Chem. Phys., 15(10), 5485–5500, doi:10.5194/acp-15-5485-2015, 2015.

Buck, A. L.: New Equations for Computing Vapor Pressure and Enhancement Factor, J. Appl. Meteorol., 20(12), 1527–1532, doi:10.1175/1520-0450, 1981.

Chazette, P. and Totems, J.: Mini N2-Raman Lidar onboard ultra-light aircraft for aerosol measurements: Demonstration and extrapolation, Remote Sens., 9(12), doi:10.3390/rs9121226, 2017.

Chazette, P., Marnas, F., Totems, J. and Shang, X.: Comparison of IASI water vapor retrieval with H2O-Raman lidar in the framework of the Mediterranean HyMeX and ChArMEx programs, Atmos. Chem. Phys., 14(18), 9583–9596, doi:10.5194/acp-14-9583-2014, 2014a.

Chazette, P., Marnas, F. and Totems, J.: The mobile Water vapor Aerosol Raman LIdar and its implication in the framework of the HyMeX and ChArMEx programs: application to a dust transport process, Atmos. Meas. Tech., 7(6), 1629–1647, doi:10.5194/amt-7-1629-2014, 2014b.

Chazette, P., Raut, J.-C. and Totems, J.: Springtime aerosol load as observed from ground-based and airborne lidars over northern Norway, Atmos. Chem. Phys., 18(17), 13075–13095, doi:10.5194/acp-18-13075-2018, 2018.

Chourdakis, G., Papayannis, A. and Porteneuve, J.: Analysis of the receiver response for a noncoaxial lidar system with fiber-optic output, Appl. Opt., 41(15), 2715, doi:10.1364/AO.41.002715, 2002.

Cooney, J.: Measurement of Atmospheric Temperature Profiles by Raman Backscatter, J. Appl. Meteorol., 11(1), 108–112, doi:10.1175/1520-0450(1972)011<0108:MOATPB>2.0.CO;2, 1972.

783 Crevoisier, C., Clerbaux, C., Guidard, V., Phulpin, T., Armante, R., Barret, B., Camy-Peyret,
784 C., Chaboureau, J.-P., Coheur, P.-F., Crépeau, L., Dufour, G., Labonnote, L., Lavanant, L.,
785 Hadji-Lazaro, J., Herbin, H., Jacquinet-Husson, N., Payan, S., Péquignot, E., Pierangelo, C.,
786 Sellitto, P. and Stubenrauch, C.: Towards IASI-New Generation (IASI-NG): impact of
787 improved spectral resolution and radiometric noise on the retrieval of thermodynamic,
788 chemistry and climate variables, Atmos. Meas. Tech., 7(12), 4367–4385, doi:10.5194/amt-7-
789 4367-2014, 2014.

790 Dinoev, T., Simeonov, V., Arshinov, Y., Bobrovnikov, S., Ristori, P., Calpini, B., Parlange, M.
791 and van den Bergh, H.: Raman Lidar for Meteorological Observations, RALMO – Part 1:
792 Instrument description, Atmos. Meas. Tech., 6(5), 1329–1346, doi:10.5194/amt-6-1329-2013,
793 2013.

794 Flamant, C., Chazette, P., Caumont, O., Di Girolamo, P., Behrendt, A., Totems, J., Lange, D.,
795 Fourrié, N., Brousseau, P., Augros, C., Baron, A., Cacciani, M., Comeron, A., De Rosa, B.,
796 Ducrocq, V., Genau, P., Labatut, L., Munoz-Porcar, C., Rodriguez-Gomez, A., Summa, D.,
797 Thundathil, R. and Wulfmeyer, V.: A network of water vapor Raman lidars for improving heavy
798 precipitation forecasting in southern France – Introducing the WaLiNeAs initiative, Bull.
799 Atmos. Sci. Technol., (submitted), 2021.

800 Fourrié, N., Nuret, M., Brousseau, P., Caumont, O., Doerenbecher, A., Wattrelot, E., Moll, P.,
801 Bénichou, H., Puech, D., Bock, O., Bosser, P., Chazette, P., Flamant, C., Di Girolamo, P.,
802 Richard, E. and Saïd, F.: The AROME-WMED reanalyses of the first special observation period
803 of the Hydrological cycle in the Mediterranean experiment (HyMeX), Geosci. Model Dev.,
804 12(7), 2657–2678, doi:10.5194/gmd-12-2657-2019, 2019.

805 Di Girolamo, P., Cacciani, M., Summa, D., Scoccione, A., De Rosa, B., Behrendt, A. and
806 Wulfmeyer, V.: Characterisation of boundary layer turbulent processes by the Raman lidar
807 BASIL in the frame of HD(CP)^2 Observational Prototype Experiment, Atmos. Chem. Phys.,
808 17(1), 745–767, doi:10.5194/acp-17-745-2017, 2017.

809 Hamamatsu: Characteristics of photomultiplier tubes, in Photomultiplier tubes: basics and
810 applications, third edition, Hamamatsu Photonics K.K. Electron Tube Division. [online]
811 Available from: https://www.hamamatsu.com/resources/pdf/etd/PMT_handbook_v3aE-
812 Chapter4.pdf (Accessed 29 April 2021), 2007.

813 Hammann, E., Behrendt, A., Le Mounier, F. and Wulfmeyer, V.: Temperature profiling of the
814 atmospheric boundary layer with rotational Raman lidar during the HD(CP)^2 Observational
815 Prototype Experiment, Atmos. Chem. Phys., 15(5), 2867–2881, doi:10.5194/acp-15-2867-

34

816   2015, 2015.

817   Hayden Smith, W. and Smith, K. M.: A polarimetric spectral imager using acousto-optic

818   tunable filters, Exp. Astron., 1(5), 329–343, doi:10.1007/BF00454329, 1990.

819   Hicks-Jalali, S., Sica, R. J., Martucci, G., Maillard Barras, E., Voirin, J. and Haefele, A.: A

820   Raman lidar tropospheric water vapour climatology and height-resolved trend analysis over

821   Payerne, Switzerland, Atmos. Chem. Phys., 20(16), 9619–9640, doi:10.5194/acp-20-9619-

822   2020, 2020.

823   IPCC: Climate Change 2013: The Physical Science Basis. Contribution of Working Group I to

824   the Fifth Assessment Report of the Intergovernmental Panel on Climate Change, edited by T.

825   F. Stocker, D. Qin, G.-K. Plattner, M. Tigno, S. K. Allen, J. Boschung, A. Nauels, Y. Xia, V.

826   Bex, and P. M. Midgley, Cambridge University Press, Cambridge., 2013.

827   Kuze, H., Kinjo, H., Sakurada, Y. and Takeuchi, N.: Field-of-view dependence of lidar signals

828   by use of Newtonian and Cassegrainian telescopes, Appl. Opt., 37(15), 3128,

829   doi:10.1364/AO.37.003128, 1998.

830   Lange, D., Behrendt, A. and Wulfmeyer, V.: Compact Operational Tropospheric Water Vapor

831   and Temperature Raman Lidar with Turbulence Resolution, Geophys. Res. Lett., 46(24),

832   14844–14853, doi:10.1029/2019GL085774, 2019.

833   Martucci, G., Navas-Guzmán, F., Renaud, L., Romanens, G., Gamage, S. M., Hervo, M.,

834   Jeannet, P. and Haefele, A.: Validation of pure rotational Raman temperature data from the

835   Raman Lidar for Meteorological Observations (RALMO) at Payerne, Atmos. Meas. Tech.,

836   14(2), 1333–1353, doi:10.5194/amt-14-1333-2021, 2021.

837   Navas-Guzmán, F., Martucci, G., Collaud Coen, M., Granados-Muñoz, M. J., Hervo, M.,

838   Sicard, M. and Haefele, A.: Characterization of aerosol hygroscopicity using Raman lidar

839   measurements at the EARLINET station of Payerne, Atmos. Chem. Phys., 19(18), 11651–

840   11668, doi:10.5194/acp-19-11651-2019, 2019.

841   Newsom, R. K., Turner, D. D., Mielke, B., Clayton, M., Ferrare, R. and Sivaraman, C.:

842   Simultaneous analog and photon counting detection for Raman lidar, Appl. Opt., 48(20), 3903,

843   doi:10.1364/AO.48.003903, 2009.

844   Prunet, P., Thépaut, J.-N. and Cassé, V.: The information content of clear sky IASI radiances

845   and their potential for numerical weather prediction, Q. J. R. Meteorol. Soc., 124(545), 211–

846   241, doi:10.1002/qj.49712454510, 1998.

847 Sherlock, V., Garnier, A., Hauchecorne, A. and Keckhut, P.: Implementation and Validation of

848 a Raman Lidar Measurement of Middle and Upper Tropospheric Water Vapor, Appl. Opt.,

849 38(27), 5838, doi:10.1364/AO.38.005838, 1999.

850 Sicard, M., Chazette, P., Pelon, J., Won, J. G. and Yoon, S.-C.: Variational method for the

851 retrieval of the optical thickness and the backscatter coefficient from multiangle lidar profiles,

852 Appl. Opt., 41(3), 493, doi:10.1364/AO.41.000493, 2002.

853 Simeonov, V., Larcheveque, G., Quaglia, P., van den Bergh, H. and Calpini, B.: Influence of

854 the photomultiplier tube spatial uniformity on lidar signals, Appl. Opt., 38(24), 5186,

855 doi:10.1364/AO.38.005186, 1999.

856 Totems, J. and Chazette, P.: Calibration of a water vapour Raman lidar with a kite-based

857 humidity sensor, Atmos. Meas. Tech., 9(3), 1083–1094, doi:10.5194/amt-9-1083-2016, 2016.

858 Totems, J., Chazette, P. and Raut, J.-C.: Accuracy of current Arctic springtime water vapour

859 estimates, assessed by Raman lidar, Q. J. R. Meteorol. Soc., 145(720), doi:10.1002/qj.3492,

860 2019.

861 Vaughan, G., Wareing, D. P., Pepler, S. J., Thomas, L. and Mitev, V.: Atmospheric temperature

862 measurements made by rotational Raman scattering, Appl. Opt., 32(15), 2758,

863 doi:10.1364/AO.32.002758, 1993.

864 Wandinger, U. and Ansmann, A.: Experimental determination of the lidar overlap profile with

865 Raman lidar, Appl. Opt., 41(3), 511, doi:10.1364/AO.41.000511, 2002.

866 Weng, M., Yi, F., Liu, F., Zhang, Y. and Pan, X.: Single-line-extracted pure rotational Raman

867 lidar to measure atmospheric temperature and aerosol profiles, Opt. Express, 26(21), 27555,

868 doi:10.1364/OE.26.027555, 2018.

869 Whiteman, D. N.: Examination of the traditional Raman lidar technique I Evaluating the

870 temperature-dependent lidar equations, Appl. Opt., 42(15), 2571, doi:10.1364/AO.42.002571,

871 2003.

872 Whiteman, D. N., Melfi, S. and Ferrare, R.: Raman lidar system for the measurement of water

873 vapor and aerosols in the Earth's atmosphere, Appl. Opt., 31(16), 3068–82,

874 doi:10.1364/AO.31.003068, 1992.

875 Whiteman, D. N., Cadirola, M., Venable, D., Calhoun, M., Miloshevich, L., Vermeesch, K.,

876 Twigg, L., Dirisu, A., Hurst, D., Hall, E., Jordan, A. and Vömel, H.: Correction technique for

877 Raman water vapor lidar signal-dependent bias and suitability for water vapor trend monitoring

878   in the upper troposphere, Atmos. Meas. Tech., 5(11), 2893–2916, doi:10.5194/amt-5-2893-
879   2012, 2012.

880   WMO: WMO Oscar : List of all requirements, [online] Available from: https://www.wmo-
881   sat.info/oscar/requirements (Accessed 28 April 2021), 2017.

882   Wulfmeyer, V., Hardesty, M. R., Turner, D. D., Behrendt, A., Cadeddu, M. P., Di Girolamo,
883   P., Schlüssel, P., Baelen, J. Van and Zus, F.: A review of the remote sensing of lower
884   tropospheric thermodynamic profiles and its indispensable role for the understanding and the
885   simulation of water and energy cycles, Rev. Geophys., 819–895, doi:10.1002/2014RG000476,
886   2015.

887